AGU PUBLICATIONS

Water Resources Research

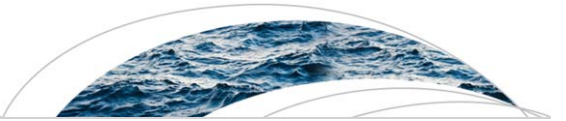

RESEARCH ARTICLE

10.1002/2016WR020339

Monitoring and simulation of salinity changes in response to tide and storm surges in a sandy coastal aquifer system

S. Huizer[1,2], M. C. Karaoulis[2], G. H. P. Oude Essink[1,2], and M. F. P. Bierkens[1,2]

[1]Department of Physical Geography, Utrecht University, Utrecht, Netherlands, [2]Department of Subsurface and Groundwater Systems, Deltares, Utrecht, Netherlands

Key Points:
- Monitoring effects of tides and storm surges on groundwater salinity with time-lapse electrical resistivity tomography
- Observed changes in salinity can be reproduced with a variable-density groundwater model
- Incorporation of wave run-up substantially improves the estimation of the extent of land-surface inundations

Supporting Information:
- Supporting Information S1
- Movie S1
- Movie S2

Correspondence to:
S. Huizer,
s.huizer@uu.nl

Citation:
Huizer, S., M. C. Karaoulis, G. H. P. Oude Essink, and M. F. P. Bierkens (2017), Monitoring and simulation of salinity changes in response to tide and storm surges in a sandy coastal aquifer system, *Water Resour. Res.*, *53*, doi:10.1002/2016WR020339.

Received 29 DEC 2016
Accepted 1 JUL 2017
Accepted article online 13 JUL 2017

Abstract Tidal dynamics and especially storm surges can have an extensive impact on coastal fresh groundwater resources. Combined with the prospect of sea-level rise and the reliance of many people on these resources, this demonstrates the need to assess the vulnerability of coastal areas to these threats. In this study, we investigated the impact of tides and storm surges on coastal groundwater at a pilot location on the Dutch coast (viz., the Sand Engine). To monitor changes in groundwater salinity under a variety of conditions, we performed automated measurements with electrical resistivity tomography for a period of 2 months between November 2014 and January 2015. The obtained resistivity images were converted to salinity images, and these images served effectively as observations of the impact of tidal fluctuations, salt-water overwash during storm surges, and the recovery of the freshwater lens after land-surface inundations. Most of the observed changes in groundwater head and salinity could be reproduced with a two-dimensional variable-density groundwater flow and salt transport model. This shows that groundwater models can be used to make accurate predictions of the impact of tides and storm surges on fresh groundwater resources, given a thorough understanding of the (local) system. Comparisons of measurements and model simulations also showed that morphological changes and wave run-up can have a strong impact on the extent of land-surface inundations in (low-elevation) dynamic coastal environments, and can therefore substantially affect coastal fresh groundwater resources.

Plain Language Summary Most coastal regions in the world rely on groundwater as their main source of fresh water. The availability of fresh water in many coastal communities is threatened by population growth, sea-level rise, and increases in the number and intensity of storm surges. This threat raises the importance of an optimal management of fresh groundwater in coastal areas to limit the salinization of fresh groundwater resources. However, the management of coastal groundwater is often complex and data is limited. In this research we have successfully used electrical resistivity tomography to measure effect of tides and storm surges on fresh groundwater at a pilot location on the Dutch coast (called the Sand Engine). In addition, most of the measured changes in groundwater head and salinity could be imitated with a numerical groundwater model. This proved that with a thorough understanding of the local system, groundwater models can be used to make accurate predictions of the impact of tides and storm surges on fresh groundwater resources.

1. Introduction

Most coastal regions in the world rely on groundwater as their main source of fresh water for agricultural, domestic, and industrial sectors. However, in many coastal regions, the availability of fresh groundwater is threatened by unsustainable levels of groundwater extraction and rising sea-levels [*Ferguson and Gleeson*, 2012]. Combined with the likely continuation of sea-level rise (SLR) and increase in the frequency and intensity of storm surges [*Nicholls*, 2010; *Wong et al.*, 2014], this will lead to more seawater intrusion (SWI) in coastal aquifers. One important driver of the increase in SWI will consist of more extensive and frequent land-surface inundations (LSI) [*Ketabchi et al.*, 2016]. In particular (low-elevation) coastal groundwater systems with shallow groundwater levels are vulnerable in this respect, because these systems are most susceptible to LSI and SWI [*McGranahan et al.*, 2007], and an increase of the groundwater level in response to SLR is restricted [*Michael et al.*, 2013].

These threats and the reliance of many coastal communities on fresh groundwater raise the importance of an optimal management of fresh groundwater in coastal aquifers to control or mitigate salinization [*Khan et al.*, 2015]. However, the management of coastal groundwater can be complex, because the extent of LSI and SWI depends on many factors: e.g., groundwater extractions, aquifer hydraulic properties, and coastal hydrodynamics and morphodynamics [*Ferguson and Gleeson*, 2012; *Vallejos et al.*, 2014]. Several studies have therefore stressed the importance of intensive monitoring, to acquire more data in different hydrogeological conditions and in real-world coastal aquifers [*Werner et al.*, 2013; *Ketabchi et al.*, 2016].

A promising monitoring technique for LSI and SWI in coastal aquifers is (time-lapse) electrical resistivity tomography (ERT) [*de Franco et al.*, 2009; *Ogilvy et al.*, 2009; *Henderson et al.*, 2010; *Morrow et al.*, 2010; *Hermans et al.*, 2012]. In ERT, the noninvasive direct current (DC) resistivity method is used to visualize the subsurface resistivity distribution in two or three-dimensional images [*Revil et al.*, 2012]. One of the main advantages of this method is the ability to conduct automated time-lapse measurements along multidimensional arrays, and therefore to provide images of the evolution of the fresh-salt groundwater distributions over time [*Ogilvy et al.*, 2009]. Additionally this technique can help to constrain or validate parameters in groundwater models [*Comte and Banton*, 2007; *Nguyen et al.*, 2009; *Beaujean et al.*, 2014].

Many studies have addressed the possible effects of climate change and in particular SLR on coastal groundwater resources [*Oude Essink et al.*, 2010; *Watson et al.*, 2010; *Chang et al.*, 2011; *Webb and Howard*, 2011; *Michael et al.*, 2013]. Most of these studies have neglected LSI [*Ataie-Ashtiani et al.*, 2013], and recent studies have shown that LSI can have a significant impact on SWI in coastal aquifers [*Ketabchi et al.*, 2014; *Morgan and Werner*, 2014]. LSI is primarily driven by coastal forcing (Figure 1), ranging from tidal fluctuations with a small to negligible impact on the mixing zone, to episodic events such as storm surges that can lead to significant SWI [*Ataie-Ashtiani et al.*, 1999; *Wilson et al.*, 2011]. Many laboratory and modeling studies have examined the impact of coastal hydrodynamics and morphodynamics on aquifers [*Robinson et al.*, 2007a; *Kuan et al.*, 2012; *Liu et al.*, 2012; *Yang et al.*, 2013; *Holding and Allen*, 2015; *Levanon et al.*, 2016]. However, only a few studies have compared model simulations with real-world measurements over an entire lunar cycle [*Abarca et al.*, 2013; *Heiss and Michael*, 2014]. These studies have demonstrated that tides create complex flow patterns.

Coastal forcing can also lead to significant changes in coastal geomorphology, e.g., migration of sandbars or coastal erosion [*Anthony*, 2013]. Complex fluid and sediment interactions, such as interactions between breaking waves, wave run-up and run-down, and groundwater flow in the swash zone, strongly determine the accretion or erosion rate of a coastal beach [*Bakhtyar et al.*, 2009]. The resulting cross-shore and alongshore morphological evolution of a coast can have large influences on the extent of SWI and LSI [*Ataie-Ashtiani et al.*, 2013; *Zhang et al.*, 2016].

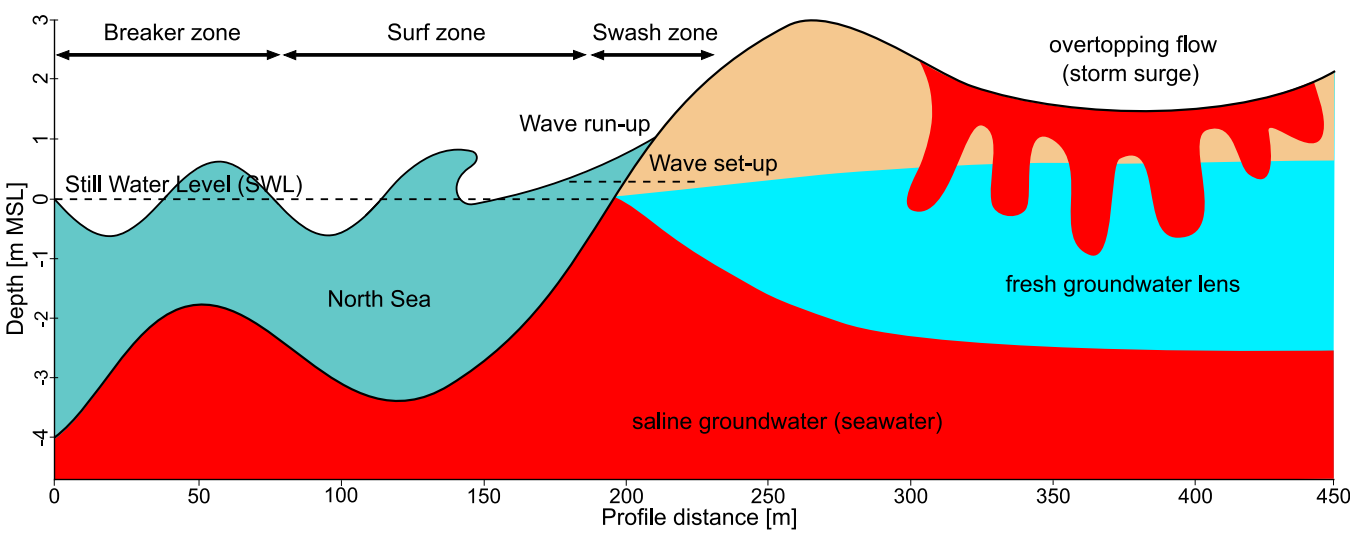

Figure 1. Illustration of coastal flow processes at the measurement site.

In this study, we investigated the impact of coastal hydrodynamics and morphodynamics on coastal groundwater with geophysical measurements and model simulations during the winter of 2014–2015. We have used time-lapse ERT to perform automated measurements of changes in the fresh-salt groundwater distribution in a mega-nourishment pilot called the Sand Engine, located in the Netherlands [*Mulder and Tonnon*, 2011]. The aim of this study is to examine the impact of coastal forcing on the fresh-salt groundwater distribution, to evaluate the quality of time-lapse ERT as a monitoring method of LSI and SWI in coastal aquifers, and to assess the ability of a variable-density groundwater and coupled salt transport model to simulate the observed variability and change. For the evaluation of time-lapse ERT as a monitoring method, we have performed sensitivity analysis and synthetic modeling as described in *Henderson et al*. [2010].

The most innovative aspect of this study is that we combined intensive monitoring of SWI and LSI with detailed model simulations over a period of several months. The morphodynamic environment of the measurement area resulted in the measurement of the impact of tides, storm surges, and coastal geomorphological changes on the fresh-salt groundwater distribution in a real-world coastal aquifer. The paper first briefly describes the study site and monitoring setup, and then provides an overview of the key results from time-lapse ERT measurement. Next, the model setup, calibration, and results are described, evaluated, and discussed, emphasizing on the quality of ERT measurements for the monitoring of SWI processes.

2. Data and Methods

2.1. Study Site: The Sand Engine

The Sand Engine (also called Sand Motor) is a pilot project that consists of the construction of a concentrated (mega) beach nourishment of 21.5 million m^3 sand at the Dutch coast in 2011 (Figure 2), and the evaluation of this new type of nourishment with respect to current practices in the Netherlands (i.e., large-scale distribution of sand). The postulated theory is that natural forces (wind, waves and currents) will gradually distribute the replenished sand along the retreating coast, support natural dune growth, and simultaneously limit the disturbance of local ecosystems. First results confirm that the mega-nourishment led to a growth of adjacent coastal sections and dunes [*de Schipper et al*., 2016]. In addition, recent research showed that concentrated mega-nourishments can lead to an increase of local fresh groundwater resources [*Huizer et al*., 2016].

In the study area, the primary source of fresh groundwater is precipitation, which was on average 938 mm per year in the period June 2011 until May 2016. Another important source of fresh groundwater is the

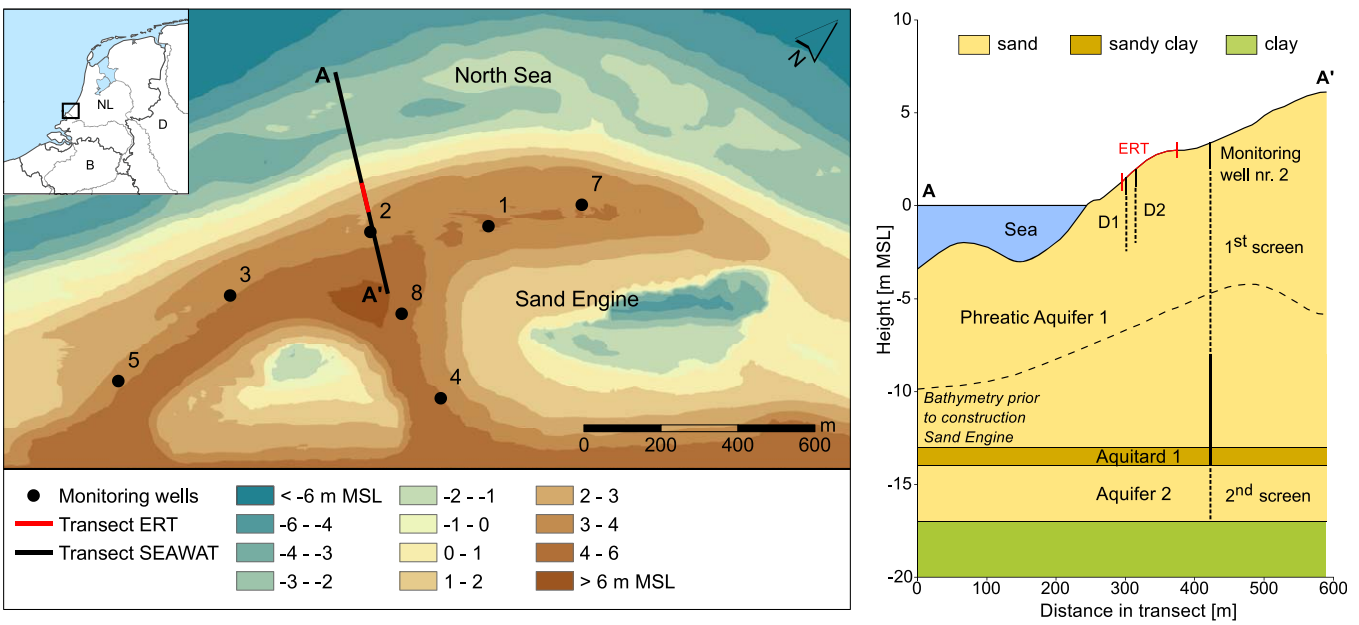

Figure 2. Contour map and hydrogeological cross section of the Sand Engine between 27 October and 1 November 2014, with the location of the monitoring wells, ERT measurement transect (red line), and the groundwater model transect (black line, A – A'). The dashed line in the cross section marks the bathymetry prior to the construction of the Sand Engine.

inflow of groundwater from the adjacent dune area Solleveld through the unconfined coastal aquifer. In general this coastal aquifer consists of 15–25 m fine to coarse sand (median grain size of 150–400 μm), with a few thin discontinuous clay layers, and is separated from underlying aquifers by a layer of clay and peat (Figure 2). Groundwater head measurements in the dunes and previous model simulations of the area [*Huizer et al*., 2016] indicate that groundwater flows downward through this aquitard. Groundwater level measurements in monitoring wells 1–8 (Figure 2) on the Sand Engine show no long-term trend, which suggests that the initial effect of the nourishment on groundwater heads is currently small or absent. However, the volume of fresh groundwater resources seems to be gradually increasing in the study area, and in the remainder of this paper we have investigated the impact of tides and storm surges on these resources.

2.2. Resistivity Imaging (ERT)

Most applications of ERT are based on the analysis of contrasts in the electrical resistivity of sediments or fluids to monitor processes in porous media [*Kuras et al*., 2009]. In this case, the contrasts in the electrical resistivity are primarily caused by differences in water content, and groundwater salinity. The measurement of the DC resistivity is based on the injection of an electrical current in the ground with multielectrode arrays and measurement of the potential differences in the other electrodes. An increase in the distance between electrodes reduces the spatial resolution and enlarges the depth of investigation, while different pairs of injection electrodes along the profile line allow imaging of the resistivity distribution of the subsurface.

2.2.1. Measurement Setup

We conducted automated time-lapse ERT measurements from 14 November 2014 10:58 until 20 January 2015 10:23, along an 80 m transect at the outer perimeter of the Sand Engine (Figure 2), situated perpendicular to the shoreline (i.e., cross-shore direction). The surface elevation along the transect varied from +1 to +3 m MSL, encompassing the local mean high water (MHW) height of +1.09 m MSL at the site (Figure 3). Alongside this transect two monitoring wells (D1 and D2) were installed for the measurement of groundwater heads and groundwater conductivity (Figure 2). This specific location was selected for three reasons: (1) the local topography was relatively simple and similar along the shoreline; (2) field data and model simulations indicate that the dominant groundwater flow direction was cross-shore, and therefore parallel to the transect; and (3) this section of the Sand Engine was most vulnerable to LSI. The 2-D measurement setup requires a (predominantly) parallel direction of groundwater flow and LSI, to avoid a misinterpretation of observed changes in the resistivity images.

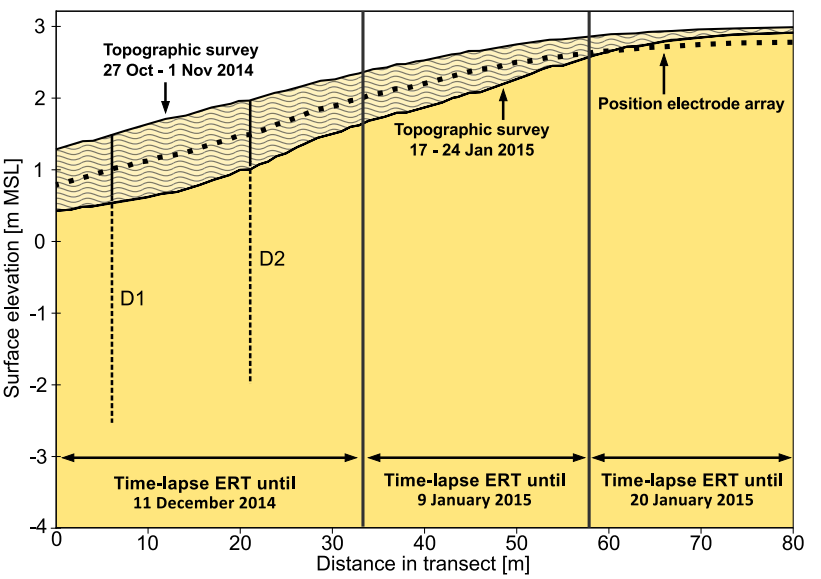

Figure 3. Cross section of the ERT measurement transect containing the implemented consecutive model surface elevations, where the wave-shading pattern indicates the erosion of sand in the measurement period. The horizontal arrows and vertical black lines mark the reduction of the ERT measurement transect on 12 December 2014 and 10 January 2015.

For all ERT measurements, the dipole-dipole configuration was implemented, which is a conventional and frequently used configuration in surveys since it is sensitive to lateral changes while the acquisition time is fast, something of importance in time-lapse studies. The measurement setup consisted of 160 electrodes with a constant spacing of 0.5 m between each electrode. Each electrode was connected to an iron pin—located at the same position and depth as the electrode—with a stainless steel wire. All electrodes were buried in a trench with a depth of 0.3–0.5 m below surface, for public health and safety and to protect the electrodes from coastal forcing and vandalism. The measurements were carried out and controlled with the MPT DAS-1 Electrical Impedance Tomography System, which was placed (with all related equipment) in an elevated and locked container to protect the instruments. The system was connected with another buried electrical cable to the electricity network in the Argus (video sampling) station, which is located in the center of the Sand Engine [*Rutten et al*., 2017]. In addition, the system was connected to the Internet with the MRD-350 industrial mobile broadband (3G router), to be able to remotely monitor and control the measurements.

However, substantial coastal erosion during the measurement period (Figure 3) led to the exposure segments of the electrode array, and consequently broken electrode connections. This rendered lower sections of the electrode array unusable, and therefore the number of available electrodes dropped during the measurements (Figure 3): all 160 electrodes were employed until 11 December 2014, 96 electrodes until 9 January 2015, and 47 electrodes until 20 January 2015. In order to maximize the number of measurements, the time interval between measurements was reduced in accordance with the decline in electrodes. Until 23 December 2014, the measurements were conducted with an interval of 30 min, from 24 December 2014 to 13 January 2015 19:00 with an interval of 15 min, from 13 January 2015 19:00 to 20 January 2015 with an interval of 10 min. This coastal erosion also affected the measurements in monitoring well D1 and D2, and reliable groundwater level and groundwater conductivity measurements could only be obtained until 19 December 2014.

2.2.2. Resistivity Inversion

All resistivity measurements were inverted with the four-dimensional (4-D) inversion algorithm as described by *Kim et al*. [2009, 2013], and *Karaoulis et al*. [2011], where inversion is the procedure to go from the measured data to an inverted resistivity image, also called a tomogram. In this algorithm both data and model are defined in space-time coordinates, and regularizations in both space and time domains are adopted to reduce inversion artifacts and to stabilize the inversion. The objective function consists of three terms that are minimized in a trade-off manner: data misfit, model roughness in the space domain, and model roughness in the time domain [*Kim et al*., 2009]. The minimization is expressed either in terms of the L1 norm or the L2 norm, and the selection of the norm is dependent on the behavior of the data and the inverse model parameters [*Kim et al*., 2013].

The inversion was conducted sequentially with five monitoring surveys or reference time steps in each inversion, and every inversion used homogeneous half-space as the starting model. The inversion model consisted of 159 columns with a constant spacing of 0.5 m, and 9 layers with a variable thickness of 0.167–0.833 m. All minimizations were expressed in terms of the L2 norm (i.e., full least-squares minimization), and the inversion of the model roughness in the space domain was conducted with a constant Lagrangian multiplier of 0.1. In addition, negative apparent resistivities and one electrode (and related electrode combinations) with a continuously high contact resistance where excluded from the inversion. All resulting unweighted and weighted RMS errors in the inversion process remained below 1%.

2.2.3. Salinity-Conductivity Relationship

For the comparison of the inverted electrical resistivities with model simulated salinities, we estimated the salinity (expressed in total dissolved solids—TDS) from the inverted bulk electrical resistivities (ρ in Ohm m) using a similar procedure as described in *Post* [2012] and *Hermans et al*. [2012]. First the groundwater resistivity (ρ_w in Ohm m), and inversely the groundwater conductivity (σ_w in S m^{-1}) was estimated from the bulk resistivity with a variant of the classical *Waxman and Smits* [1968] model. The cation exchange capacity in this model was ignored, because the clay fraction in the upper part of the sand nourishment is negligible (Figure 2). This reduces the model to a simple linear relation:

$$\rho = \rho_w \cdot \frac{F}{{s_w}^n}; \quad \sigma = \sigma_w \cdot \frac{{s_w}^n}{F} \tag{1}$$

where F is the electrical formation factor of the sediment, s_w is the relative water saturation, and n is the saturation exponent.

The focus of this research was limited to the saturated zone, and thus s_w was constrained to a value of 1. Estimated salinities in the unsaturated zone were therefore excluded from the analysis of the effect of tides and storm surges. The formation factor was also estimated with equation (1), i.e., equal to the ratio between the groundwater conductivity and the bulk conductivity (σ in S m^{-1}): on-site measurements of the groundwater conductivity between 14 November 2014 10:58 and 11 December 2014 03:57 in monitoring well D1 (Figure 3) at a depth of −0.5 m MSL were divided by the inverted bulk conductivity at the same approximate position. Ignoring anomalous conductivities, this resulted in an average formation factor of 4.2 in this period with a standard deviation of 0.3, which is similar to literature values for coarse sand [*Friedman*, 2005; *Goes et al*., 2009]. The variability in the formation factor was mainly a result of fluctuations in the on-site measured groundwater conductivity, and a gradual decline in only the inverted bulk conductivity. Possibly the water inside monitoring well D1 was more sensitive to LSI, which led to a larger response in conductivity and the absence of a (clear) falling trend.

Groundwater salinities were estimated with the salinity-conductivity relationship as defined in the algorithm of the Practical Salinity Scale (PSS) 1978 [*Fofonoff and Millard Jr*., 1983]. This so-called Practical Salinity S_p is a dimensionless measure of salinity, which is defined in terms of the ratio with the conductivity of standard seawater ($S_p = 35$) at a temperature of 15°C, and at atmospheric pressure. The calculation of S_p is dependent on the electrical conductivity, the temperature, and (water) pressure at depth of the measurement [*IOC et al*., 2010]. Temperatures were estimated with measurements in monitoring well 2 at a depth of −0.2 m MSL (Figure 2), which dropped from 13.8°C on 14 November 2014 to 10.6°C on 20 January 2015. Deviations from atmospheric pressure were ignored in the calculations, because the observed variations in atmospheric pressure have negligible effects on the S_p. The PSS 1978 is only defined for salinities in the range $2 < S_p < 42$. Consequently, for salinities between 0 and 2 the extension of the PSS 1978 as defined by *Hill et al*. [1986] was adopted. The dimensionless values for S_p were converted to salinities in g TDS L^{-1}, with the relationship between the chloride concentration and the Practical Salinity as described in *Millero et al*. [2008].

2.3. Variable-Density Groundwater Flow Model

For the analysis of the observed changes in groundwater head and salinity in the fresh-salt groundwater mixing zone, we developed a 2-D variable-density groundwater model with a horizontal spacing of 0.2 m and vertical spacing of 0.2 m. Variable-density saturated groundwater flow and coupled salinity transport were simulated with the computer code SEAWAT [*Langevin et al*., 2008]. The governing flow and solute transport equations in SEAWAT are coupled and solved with a cell-centered finite difference approximation. Numerous studies have used this model code to simulate variably-density, transient groundwater flow in coastal environments [*Mao et al*., 2006; *Robinson et al*., 2007b; *Heiss and Michael*, 2014; *Pauw et al*., 2014]. Pressure heads and saturation levels in the unsaturated zone will have an important impact on infiltration rates, however in this research we have focused on processes in the saturated zone. In the simulations we have assumed that the infiltration of freshwater by precipitation and seawater by LSI occur instantaneously. We believe this choice is justified because of the high infiltration rates of the coarse sand, and the relatively shallow unsaturated zone along the measurement transect (maximum 2 m).

The groundwater flow model was situated perpendicular to the shoreline, alongside the ERT measurement transect (Figure 2). Based on four boreholes with a depth of 20 m below surface, situated 7–400 m from the model transect, we modeled two aquifers and one aquitard (see cross section in Figure 2). The aquifers contain fine-grained to medium coarse-grained sand and occasionally shells, and the aquitard consist of sandy clay to clay.

2.3.1. Initial Conditions

The groundwater head and salinity distribution at the start of the time-lapse ERT measurement were reconstructed with model simulations from the completion of the Sand Engine in June 2011 until the start of the measurements in November 2014. The initial distribution of the groundwater salinity in the model was defined completely saline, i.e., equal to the average seawater salinity at the site of approximately 28 g TDS L^{-1} [*Rijkswaterstaat*, 2012]. In the intervening period, the Sand Engine experienced substantial geomorphological changes, in particular along the outer perimeter of the peninsula, where the shoreline retreated approximately 200 m [*de Schipper et al*., 2016]. These geomorphological changes of the Sand Engine were monitored with monthly to bimonthly topographic surveys (including bathymetry) as part of an intensive monitoring program. Dependent on the monitoring frequency and the extent of morphological change, we

have updated the surface elevation every 1–3 months in the model by sequential grid regenerations. For the extent of the morphological change, we used this criterion for the exclusion of topographic surveys: the maximum (horizontal) shift in the topography, above the mean neap tide height (+0.86 m MSL) and below the maximum run-up height (in the concerning period), should be smaller than 10 m. The excluded surveys (8 out of a total of 30 surveys) where either conducted in the summer season (fewer storm surges), or surveys that were conducted quickly after another (e.g., twice in 1 month).

2.3.2. Boundary Conditions

Sea-level fluctuations were based on high frequency (10 min time interval) tide gauge measurements (also called Still Water Level: SWL) in the harbors of Scheveningen and Hoek van Holland, which are located 7.5 km north and 9.3 km south from the study site. Based on the position of the study site, we used an averaged time series of both measurement sites as an estimate of the local sea-level fluctuations. This approximation was corroborated with a comparison to short-term on-site sea-level measurements between 17 September and 23 October 2014, which revealed an absolute mean error of 0.06 m and a RMSE of 0.075 m. In the model simulations, only sea-level fluctuations larger than 2 cm were incorporated, which resulted in stress periods with a variable duration of 10–190 min.

Based on the sea-level and the topography, the inundation extent was determined for every stress period, and modeled as "General Head (head-dependent) Boundaries and Drains" as described in *Mulligan et al*. [2011]. All model layers in the phreatic aquifer (Figure 2) were defined convertible (saturated thickness) and rewettable with a wetting threshold of 0.01 m [*McDonald et al*., 1992]. Despite this relatively small wetting threshold, and detail in the simulation of the sea-level fluctuations, not all model cells were reactivated in every stress period unless an additional infiltration rate was added to the simulations. This deficiency was only observed for sea-levels that were larger than the MHW height. Therefore, to ensure a reactivation of all inundated model cells, an additional infiltration of 0.008 m per minute of seawater was added to the area of inundation for sea-levels larger than the MHW height. The adopted infiltration rate was the lowest rate that led to a reactivation of all inundated model cells, and this rate equaled the drainable volume of two model layers over a 10 min period.

Besides this simulation of the SWL (model scenario S1), two additional model scenarios (S2 and S3) with estimations of, respectively, the wave setup height and the wave run-up height at the site were implemented to study and improve the resemblance of the simulations with reality (Figure 1). Wave setup is defined as the local rise of the mean seawater level (with respect to SWL), caused by wave breaking. Wave run-up is defined as the maximum level of wave up-rush on the beach (with respect to SWL), which is only exceeded by 2% of run-up events. The wave setup height $<\eta>$ and wave run-up height R_2 in every stress period were estimated with general empirical expressions [*Stockdon et al*., 2006]:

$$<\eta> = 0.35\ \beta_f (H_0 L_0)^{1/2} \tag{2}$$

$$R_2 = 1.1\left(0.35\ \beta_f (H_0 L_0)^{1/2} + \frac{\left[H_0 L_0 \left(0.563\beta_f{}^2 + 0.004\right)\right]^{1/2}}{2}\right) \tag{3}$$

where H_0 is the deep water significant wave height, L_0 is the deep water wave length, and β_f is the foreshore beach slope. The significant wave height and wave length were estimated with measurements at the "Euro platform" of the Ministry of Infrastructure and the Environment (Rijkswaterstaat), which is located 50 km southwest from the study site (Figure 4).

Wave setup (S2) was modeled similarly to the observed sea-level fluctuations (SWL), and wave run-up (S3) as the combination of wave setup and wave up-rush (Figure 1). Nonlinear effects of wave setup on the surface water level were not included, because possible seawater circulations through the aquifer will probably have a small to negligible effect on the fresh-salt groundwater distribution. Wave up-rush was modeled as an infiltration of seawater, between the wave setup height $<\eta>$ and the wave run-up height R_2. The infiltrated volume of seawater at the wave setup height $<\eta>$ was estimated—in every stress period—as the drainable storage (determined by specific yield) between SWL and $<\eta>$. Above the wave setup height $<\eta>$, this infiltration volume was reduced linearly to a value of 10% at the wave run-up height R_2. The value of 10% is a best guess that was based on the number of run-up events that reach the run-up height R_2 (generally between 1 and 3 events in 10 min), the average infiltrated volume at the wave setup height $<\eta>$ (0.013 m between June 2011 and 20 January 2015), and the assumption that at least 0.001 m infiltrates during every run-up event.

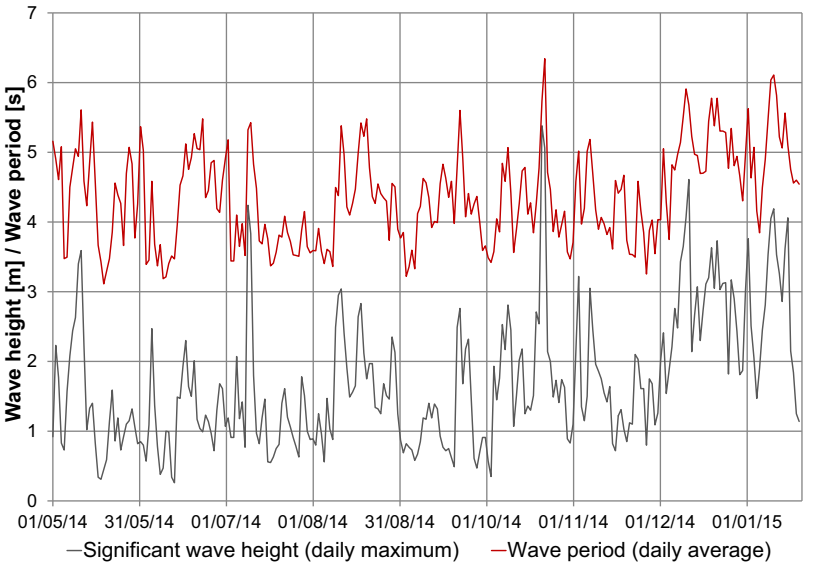

Figure 4. Measured deep water significant wave height H_0 (daily maximum) and deep water wave period (daily measured) at the "Euro platform" (50 km southwest from the study site).

The inland boundary of the model was simulated as a constant groundwater head and constant concentration boundary, where the vertical distribution and change of the groundwater head and salinity in the boundary were estimated with a separate 1-D groundwater flow model. This 1-D model consisted of the same hydrogeological properties as the calibrated 2-D model (Table 1), groundwater recharge, and the local saline groundwater head (monitoring well 8). Based on groundwater level measurements in monitoring wells 2, 4, and 8 and the local topography, we assumed that the change in groundwater salinity was predominantly determined by groundwater recharge. The local groundwater head was assigned to the bottommost model layer and defined as a variable head, equal to the daily moving average of the measured groundwater head in monitoring well 8 for the period 1 June 2014 to 20 January 2015 (Figure 2). In the preceding period, we have implemented the average groundwater head. The salinity in this bottommost layer was set equal to average seawater salinity.

Hourly measurements of precipitation and reference crop evapotranspiration at a measurement station in Hoek van Holland were used to estimate groundwater recharge. The hourly groundwater recharge was linearly distributed over smaller-sized stress periods. For the estimation of the potential soil evaporation, we used crop coefficients for bare or sandy soil [*de Bruin*, 1987; *Meinardi*, 1994; *Spieksma et al*., 1996]: 0.6 for the summer (April–September), and 0.9 for the winter (October–March). Monthly precipitation and potential soil evaporation were subtracted, in order to generate monthly estimates of the fraction of the hourly precipitation that reaches the groundwater level. It is important to note that this approach might lead to an overestimation of soil evaporation in months with prolonged dry periods, which will mainly affect the summer season and to a lesser extent the winter season.

Table 1. Calibrated Parameter Values Implemented in the Model Simulations

Layer Type	Parameter	Value
All model layers	Longitudinal dispersivity	0.02 m
	Transverse dispersivity	0.002 m
Phreatic aquifer	Horizontal hydraulic conductivity	36 m d^{-1}
1: [above −9 m MSL]	Vertical hydraulic conductivity	18 m d^{-1}
	Specific yield	0.20
Aquitard	Horizontal hydraulic conductivity	1.15×10^{-1} m d^{-1}
1: [–13 to −14 m MSL]	Vertical hydraulic conductivity	1.15×10^{-2} m d^{-1}
	Specific storage	2×10^{-4}
Aquifer	Horizontal hydraulic conductivity	36 m d^{-1}
1: [–9 to −13 m MSL]	Vertical hydraulic conductivity	7.2 m d^{-1}
2: [–14 to −17 m MSL]	Specific storage	2×10^{-4}

2.3.3 Model Calibration

The groundwater model was calibrated with measurements of the groundwater head in multilevel monitoring well 2, which is situated alongside the 2-D model (Figure 2). This monitoring well contained two well screens, situated in separate aquifers (see cross section in Figure 2). The calibration was performed with model scenarios S1, S2, and S3 (respectively SWL, wave setup, and, wave run-up), for measurements from 1 May 2014 until the start of the scenario simulations on 21 October 2014. The calibration strategy consisted of extensive sensitivity analyses, manual model parameter calibration, and comparisons of measured and simulated groundwater heads for the calibration period. In this strategy, we have adopted two calibration criteria: the error between the measured and simulated groundwater head should be smaller than the observed variation in groundwater level (average standard deviation is 0.1 m in the calibration period), and the simulated groundwater head should correlate with the observed fluctuation pattern.

The parameter calibration comprised of the manual adjustment of a selection of the most sensitive model parameters: (horizontal and vertical) hydraulic conductivity, storage coefficients, and (longitudinal and transverse) dispersivity. These adjustments consisted of small incremental changes from an initial best guess, which was based on previous model simulations in the same area [*Huizer et al*., 2016]. Other parameters such as groundwater recharge were based on measurements, and were excluded from the calibration. The longitudinal and transversal dispersivity were adapted in agreement with the observed mixing zone thickness. The calibrated set of model parameters is shown in Table 1.

2.3.4. Model Scenarios

As described in section 2.3.2, the observed SWL, estimated wave setup, and estimated wave run-up were implemented in three separate model scenarios (S1, S2, and S3), to analyze the reproducibility of the observed LSI and SWI processes in the ERT measurements. These model scenarios S1, S2, and S3 were executed for the initialization period of 1 June 2011 (completion Sand Engine) to 21 October 2014, and the study period of the 21 October 2014 to the end of the ERT measurements on 20 January 2015. The simulations were started before the ERT measurements to incorporate the storm surge that occurred between 21 October 2014 16:00 until 22 October 09:00 (significant offshore wave height of 4–5.4 m, and offshore wave period of 6.3–7.2 s). This storm surge led to the inundation of the entire measurement transect, as indicated with the highest measured SWL on the 22 October 2014 in Figure 5. This was the most intensive storm at the Sand Engine since 6 December 2013, which led to the highest seawater level and consequently the most extensive LSI of the measurement period. Other storms that occurred during the measurement

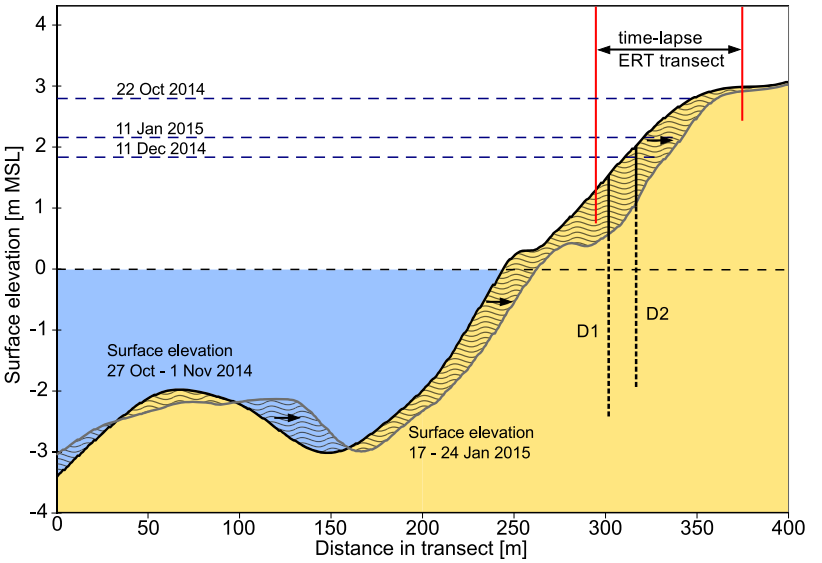

Figure 5. Cross section with the observed surface elevations at the measurement site: 27 October to 1 November 2014 (black line), and 17 to 24 January 2015 (grey line). The wave-shading pattern between the lines marks the erosion or accretion of sand in the intervening period. The red lines mark the ERT transect and the blue dashed lines mark the three highest SWL in the measurement period.

period were on 11 December 2014 (significant offshore wave height of 3–4 m, and offshore wave period of 5.5–6.5 s) and on 11 January 2015 (significant offshore wave height of 3.5–4.2 m, and offshore wave period of 5.8–6.7 s), and the highest measured seawater levels during these storms are also indicated in Figure 5.

Coastal forcing—and the earlier mentioned storm surges in particular—led to substantial morphological changes at the Sand Engine in the measurement period, as illustrated in Figure 5. This morphological change is based on two extensive topographic (including bathymetry) surveys that were conducted on the Sand Engine between 27 October 2014 and 1 November 2014, and between 17 and 24 January 2015. Each survey produced a large collection of height measurements that were spatially interpolated to obtain an estimation of the surface elevation along the model transect (Figure 5). The disparity between these surface elevations shows the retreat of the shoreline at the site during the surveys. In order to obtain an optimal correspondence in the actual and the modeled topography, the horizontal average of both surface elevations was used as an estimation of the intermediate elevation along the model transect from 12 to 31 December 2015. Before and after this period, we have adopted interpolations of the two topographic measurements (see dashed line in Figure 5).

In order to study the effect of groundwater recharge on the salinity distribution in more detail, model scenario S3 was also simulated without groundwater recharge. This simulation was only executed for the study period after the calibration (21 October 2014 to 20 January 2015), and preceding simulations of model scenario S3 were used as initial conditions.

3. Results

3.1. Groundwater Head

In most of the calibration period, the simulated groundwater head in the model scenarios closely resemble the observed fluctuation pattern, substantiating that the groundwater model accurately describes the course of the groundwater level and groundwater flow in the study site (Figure 6). The absolute mean error between the measured and simulated groundwater head of model scenario S1, S2, and S3 is, respectively, 0.06, 0.05, and 0.05 m in the phreatic aquifer (RMSE 0.07, 0.06, and 0.05 m), and respectively 0.13, 0.12, and 0.10 m in the bottom aquifer (RMSE 0.17, 0.15, and 0.13 m). Wave setup (S2) and in particular wave run-up (S3) results in larger LSI and consequently higher groundwater levels. Overall, the observed fluctuation in groundwater head can to a large extent be explained by variations in sea-level (spring tide-neap tide cycle), coastal geomorphology, groundwater recharge, and groundwater flow across the inland model boundary. The initial deviation of the groundwater head of approximately 0.20 in the bottommost aquifer—in contrast with the resemblance in the upper aquifer—is probably caused by underestimations in the inflow of groundwater across the inland model boundary in the previous period, possibly in combination with geologic differences.

Focusing on the effect of tides and storm surges, Figure 6 shows that for most LSI instances (indicated with black arrows) the simulated increase in groundwater head is similar to the measurements (e.g., on 9 and 24 September), while in some instances the model overestimates the increase in groundwater head (e.g., on 14 and 30 July). Probably the primary cause for this contrast are mismatches between the actual and modeled topography, which is a consequence of continued morphological changes between the bimonthly topographic surveys. For example, photographs of the Sand Engine from the Argus (video sampling) station indicate that a sand bar developed in the intertidal zone, after the storm surge on 9 July 2014 (Figure 4), and this sand bar could have dampened the extent of the LSI on 14 and 30 July.

As for precipitation, Figure 6 shows that precipitation led to negligible to small rises—often in the order of centimeters—in the measured groundwater level, as for example during relatively high rainfall events on 27 May (17.7 mm in 15 h) and 28 July (16.8 mm in 11 h). Because the measured precipitation was probably generally close to reality, this indicates that the volume of groundwater recharge was substantially reduced due to evaporation and storage. In most instances, the simulated response to precipitation was similar to the measured response, however in some instances (e.g., the period of high rainfall between 13 and 25 August) the simulated change in groundwater head appeared to large when compared with measurements. This suggests that either the simulated

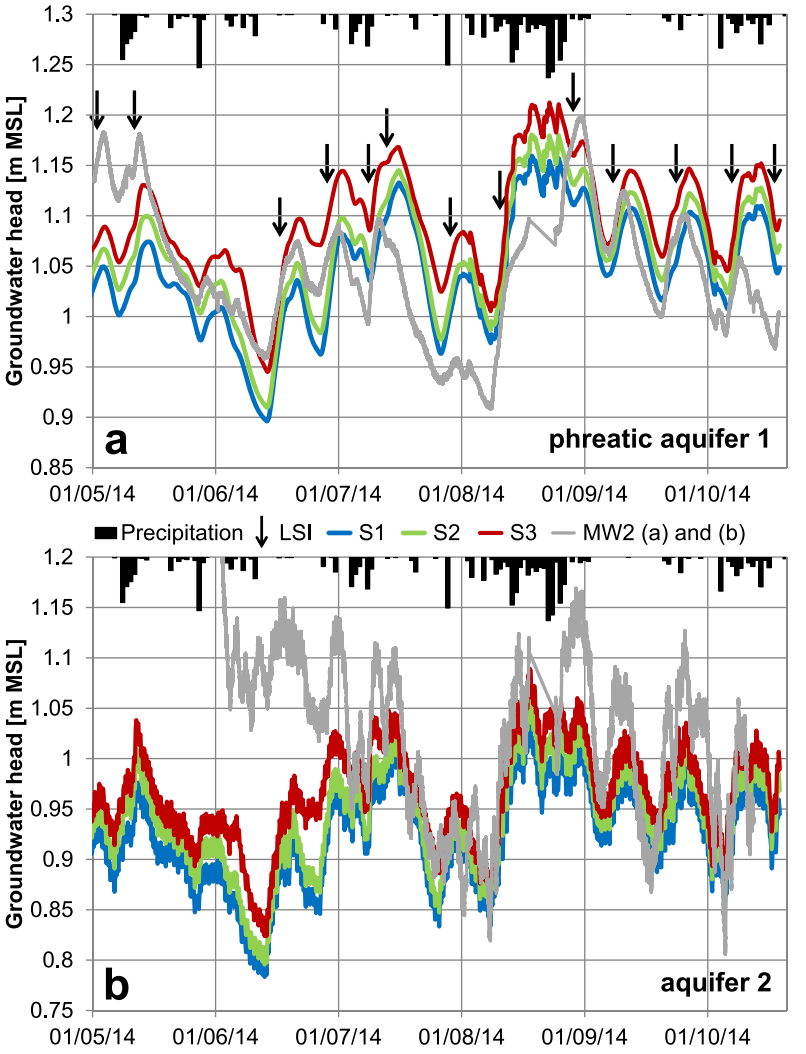

Figure 6. (a) Measured groundwater head (gray line) in the upper well screen of monitoring well 2 and (b) the lower well screen of monitoring well 2, with the simulated groundwater head of model scenario S1 (SWL, blue line), S2 (wave setup, green line), and S3 (wave run-up, red line). The vertical grey bars mark topographic surveys on the Sand Engine, the arrows mark LSI instances where the sea-level was higher than the Mean High Water Spring (MHWS) height of +1.28 m MSL, and the black bars indicate the daily precipitation (in mm d^{-1}) with a maximum of 21 mm on 22 August 2014.

evaporation in this period was underestimated, or that the volume of precipitation stored in the unsaturated zone was larger than anticipated.

The performance of the calibrated model was examined with observations of the groundwater level from 7 November to 19 December 2014, taken in monitoring well D1 and D2 (Figure 7). These observations were situated near the local MHW height of +1.09 m MSL and were therefore more exposed to sea-level fluctuations in comparison with monitoring well 2. The similarity in the observed and simulated groundwater head in this period confirms the reliability of the calibrated model at different distances from the local MHW height. The absolute mean error between the measured and simulated groundwater head of model scenario S1, S2, and S3 is respectively 0.142, 0.138, and 0.135 m for monitoring well D1 (RMSE 0.19, 0.18, and 0.17 m), and respectively 0.14, 0.13, and 0.11 m for monitoring well D2 (RMSE 0.20, 0.18, and 0.15 m).

During the first 4 weeks (7 November to 5 December), the weather conditions were generally calm with low wave heights (Figure 4), in contrast with the stormy conditions in the last 2 weeks (5–19 December). This resulted in fewer and less extensive inundations in the period before 5 December, and consequently smaller

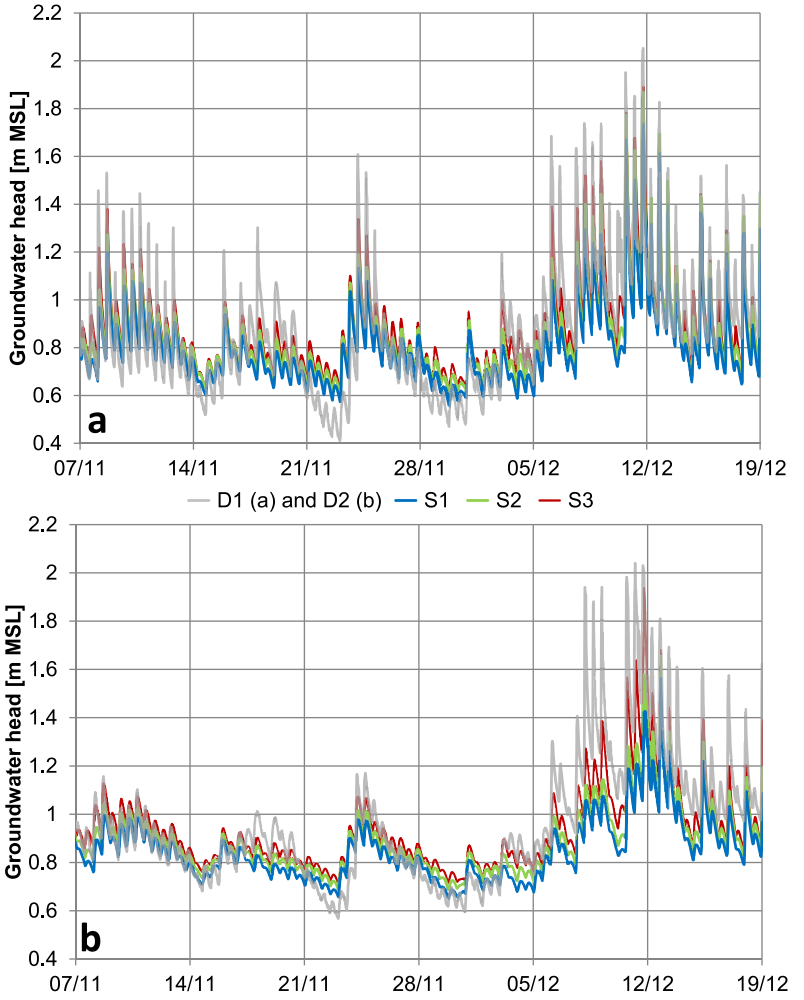

Figure 7. Measured groundwater head in monitoring well (a) D1 and (b) D2, and simulated groundwater head in model scenario S1 (SWL, blue line), S2 (wave setup, green line), and S3 (wave run-up, red line).

variations in groundwater head, and this contrast is captured in both the measured and simulated groundwater head. However, in some periods the simulated and measured groundwater head diverge, as for example between 17 and 22 November. Photographs of the study site from the Argus (video sampling) station indicate that this mismatch is probably caused by a sand bar, which (slowly) developed in the intertidal zone in this period, and this shortened or dampened the extent of inundations.

In addition, the figure shows that in many instances the response of the groundwater head to LSI is underestimated. However, comparisons of the model scenarios (Figure 7) suggest that the incorporation of wave run-up led to a small improvement in the simulation of the response of the groundwater level to coastal hydrodynamics and morphodynamics. In particular in scenario S1 (SWL), the model seems to underestimate short-term fluctuations in groundwater level, but the incorporation of wave run-up in model scenario S3 led to additional inundation height of 0.1–0.7 m.

3.2. Land-Surface Inundation (LSI)

For the analysis of the frequency and extent of LSI during the measurement period, observed instances of LSI along the ERT measurement transect were compared with the simulated LSI in model scenario S1 (SWL) and S3 (wave run-up; Figure 8). In both measurements and model simulations, we have defined the maximum extent of LSI (defined with respect to the seaward boundary of the electrode array) on the basis of

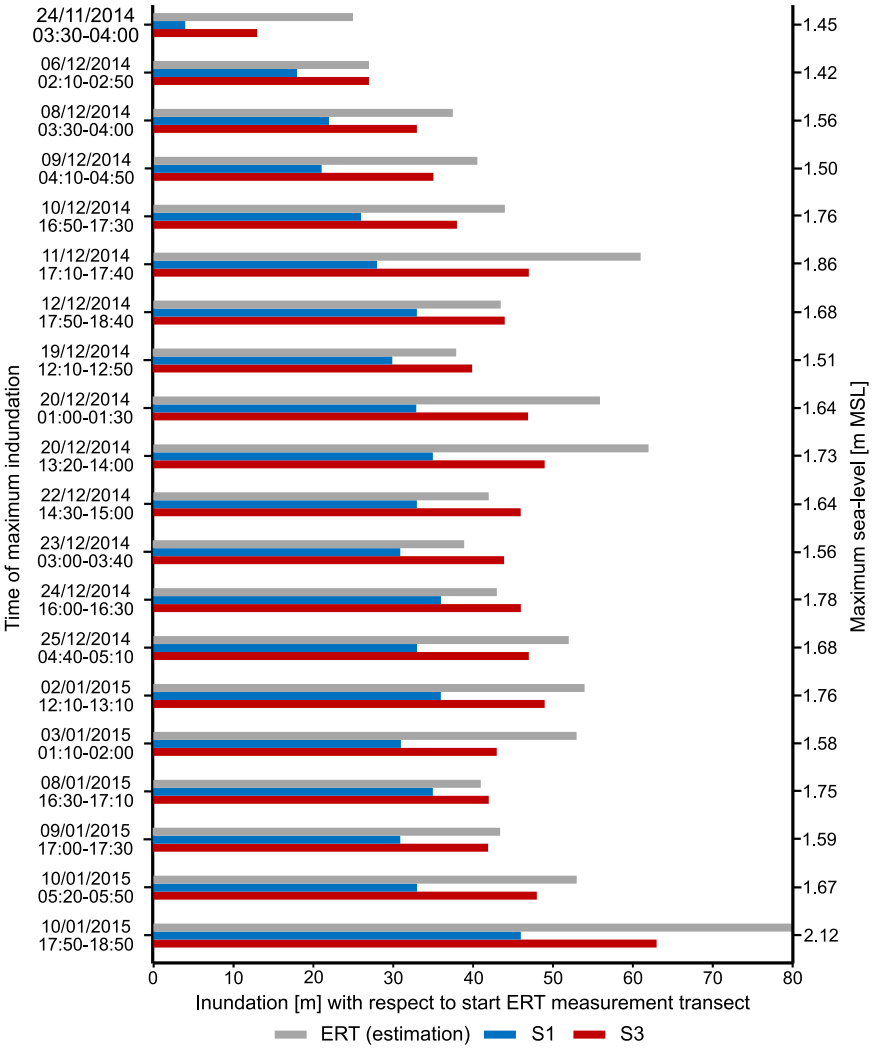

Figure 8. Maximum extent of LSI (m) along transect with respect to seaward boundary of the ERT measurement, for model scenario S1 (SWL, blue line), and S3 (wave run-up, red line).

the first substantial deviation in the resistivity or salinity (at least 100%) in the upper layers of the phreatic aquifer.

Variations in the extent of LSI (Figure 8) show that LSI are not only dependent on the sea-level, but also on the storm intensity, and (changes in) the local topography (i.e., surface elevation and morphology). Changes in the storm intensity can lead to substantial variations in wave run-up, and therefore to an extension of LSI in instances with equal sea-levels. The simulations confirm the importance of wave run-up by showing that the incorporation of wave run-up reduces the underestimation in the level of LSI and lowers the error between the measured and simulated extent of LSI in all instances. However, variations in the local topography, due to the continued retreat of the shoreline (Figure 5), can also lead to substantial shifts in the area of inundation.

3.3. Groundwater Salinity

The inverted time series of resistivity images of 14 November 2014 to 20 January 2015 were converted to salinity with the procedure that was described in section 2.2.3. In the presentation and discussion of the results, we have concentrated on these salinities to be able to differentiate between fresh, brackish, and salt groundwater, to improve the connection of changes in salinity with LSI or other processes, and to perform side-by-side comparisons with the model simulated salinities. But first this time series of interpreted

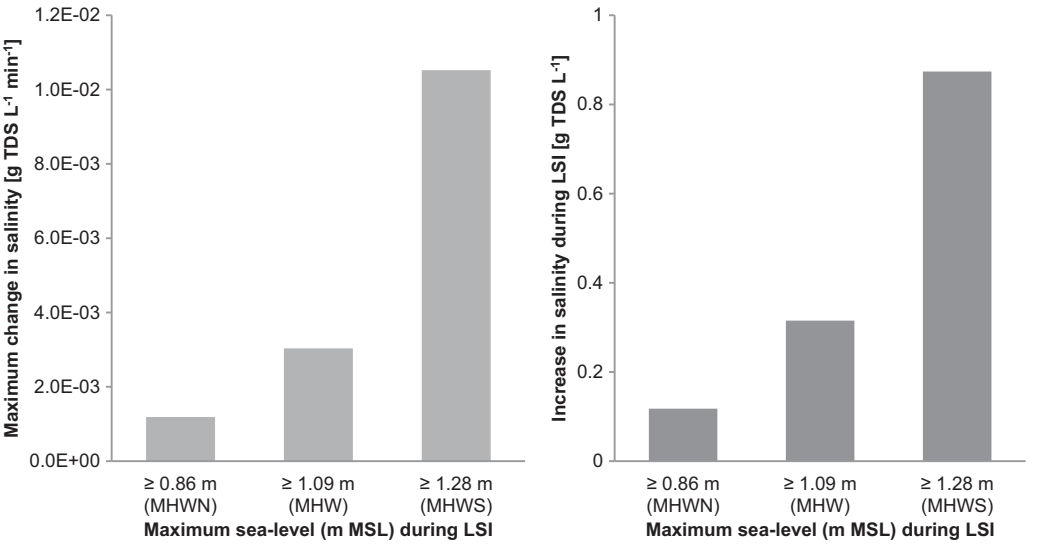

Figure 9. Average maximum increase in salinity (in g TDS L^{-1} min^{-1}) and average total increase in salinity during LSI (in g TDS L^{-1}), as observed in the ERT measurements between 14 November and 11 December 2014, grouped for LSI with sea-levels larger or equal to the MHWN, the MHW, and the MHWS.

groundwater salinities was used to investigate the effect of coastal hydrodynamics and morphodynamics on the fresh-salt groundwater distribution. In this study, we have focused on the change in groundwater salinity between the groundwater level and a depth of −1 m MSL, because the aim of this study lied on fresh groundwater resources and this depth range encompasses most of the observed changes in the fresh-salt groundwater mixing zone, and because the ERT data were most sensitive and therefore reliable near the surface (see Appendix A).

The observed changes in groundwater salinity in the measurement period show that in most instances an increase in salinity coincides with tides and storm surges, and that the impact varies with the extent of the inundation. This is illustrated in Figure 9, with the (average) maximum increase in salinity and the (average) total increase in salinity during LSI between 14 November and 11 December, for LSI with sea-levels larger or equal to +0.86 m MSL (Mean High Water Neap: MHWN), +1.09 m MSL (MHW), and +1.28 m MSL (MHWS). Decreases in salinity along the measurement transect are predominantly caused by falling groundwater levels (frequently as a consequence of LSI), and to a lesser extent by (high) rainfall events (Figure 10). However

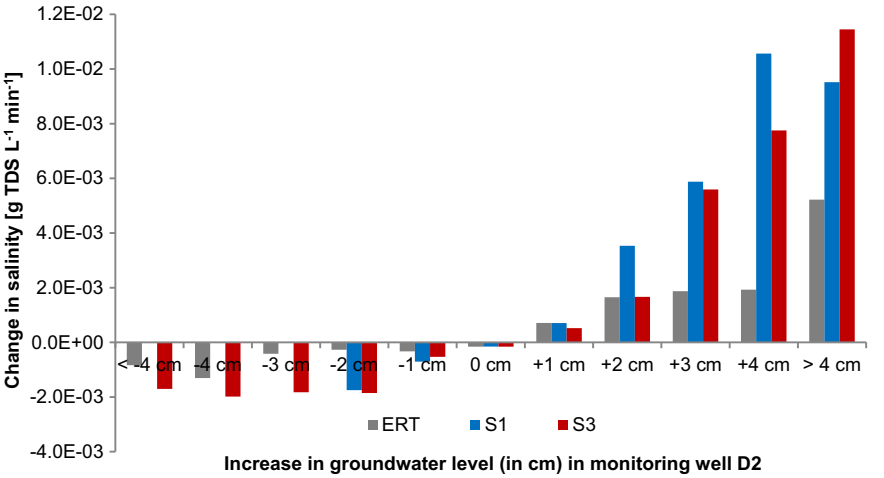

Figure 10. Average increase in groundwater salinity (in g TDS L^{-1} min^{-1}) between 14 November and 11 December 2014, as observed in the ERT measurements (gray), model scenario S1 (SWL, blue), and model scenario S3 (wave run-up, red), grouped by the measured or simulated change in groundwater head (in cm) at monitoring well D2 and sampled with a 30 min interval.

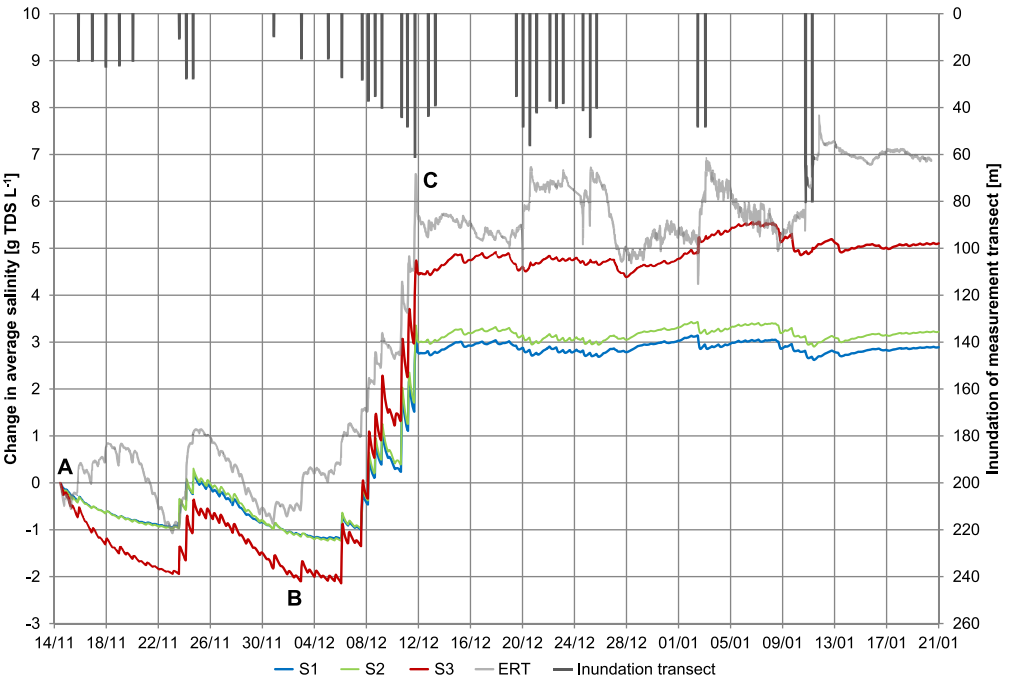

Figure 11. Change in salinity (g TDS L^{-1}) with respect to the initial salinity distribution, for the observed salinity (gray line), model scenario S1 (SWL, blue line), S2 (wave setup, green line), and S3 (wave run-up, red line). Instances of LSI (m) of (sections of) the transect are shown with dark grey bars. The letters A, B, and C mark the time of the three images shown in Figure 13.

some of the (small) changes in the measured salinity cannot be explained by LSI and recharge. Possible causes for these are small fluctuations in the electrical resistivity, measurement errors (related to disconnection of electrodes or rapid changes in resistivity), and changes in moisture content in the unsaturated zone.

For the examination of particular effects of LSI (e.g., wave run-up and recharge) on the fresh-salt groundwater distribution, we compared measured and simulated changes in groundwater salinity. The comparison of the change in salinity was conducted in two respects: first in relation to the change in groundwater salinity (Figure 10), and second in time (Figures 11 and 12) with respect to the salinity distribution on the 14 November 2014 11:00 (start of measurements). Changes in the length of the electrode array (Figure 3) were adopted in the comparison with model simulations, and only sections with reliable measurements were compared.

The overall resemblance between the measured and simulated change in groundwater salinity demonstrates—in particular for model scenario S3—that the changes in groundwater salinity along the measurement transect are primarily determined by sea-level fluctuations and associated groundwater flow (Figures 10 and 11). In addition, the contrast in the reproducibility of the observed phenomena between model scenario S1 (SWL), S2 (wave setup), and S3 (wave run-up) substantiates the importance of a reliable estimation of LSI, and in particular wave run-up.

Groundwater recharge has a small effect on the groundwater salinity in the measurement period (see Figure 12). Many differences in the measured and simulated salinity are probably caused by underestimations in the extent of LSI, e.g., the effect of inundations between 14 and 20 November, and between 20 and 24 December is underestimated (Figure 8). Other possible causes for differences between measured and simulated salinities are related to errors in the conversion of the electrical resistivity to groundwater salinity, underestimations in the fluctuation in the groundwater level (see Figure 7), or changes in measured resistivity that are related to moisture content.

Comparisons of the absolute groundwater salinity in measurements and simulations shows that the general pattern matches, with increases in salinity due to inundations and a small fresh to brackish groundwater lens on the landward side (Figure 13). The complete time-series of the measurements and simulations is included

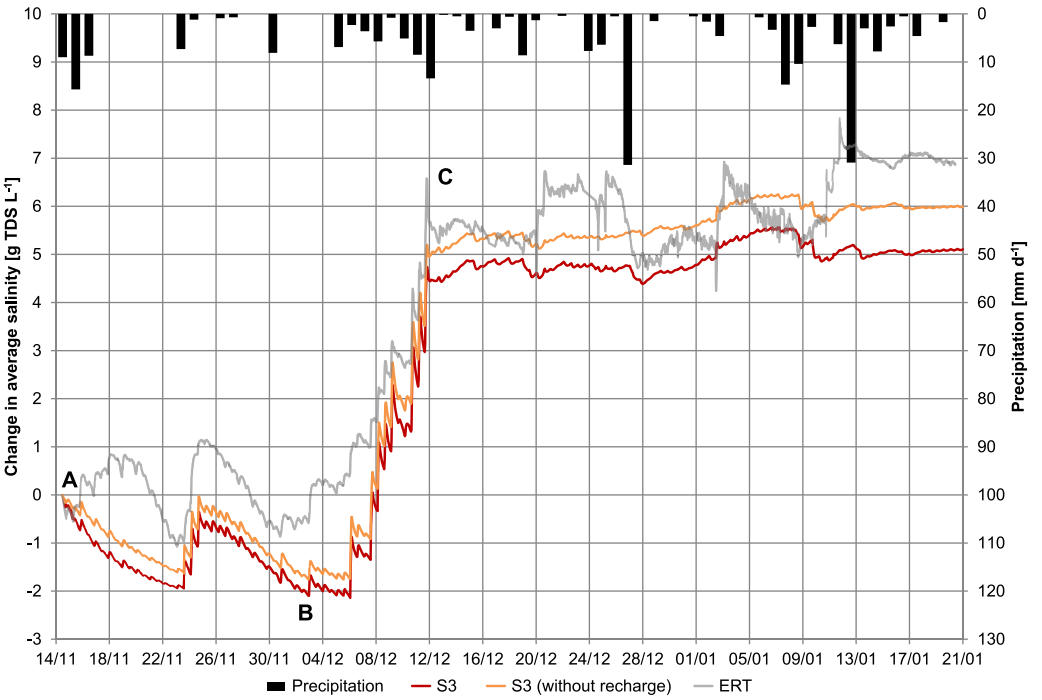

Figure 12. Change in salinity (g TDS L^{-1}) with respect to the initial salinity distribution, for the observed salinity (gray line), and model scenario S3 (wave run-up) with recharge (red line) and without recharge (orange line). The precipitation is given in mm d^{-1} with black bars. The letters A, B, and C mark the time of the three images shown in Figure 13.

as supporting information. But some groundwater salinities appear to be underestimated in the model simulations or overestimated in the converted salinities. Conversely, the groundwater salinity at the seaward side appears to be higher in the simulations. These differences are probably caused by the inversion (smoothing and artifacts, see Appendix A), errors in the conversion of the resistivity to groundwater salinity, errors in the initial salinity distribution, or mismatches in the salinization of the coastal aquifer during LSI.

4. Discussion

4.1. Imaging Groundwater Salinity With ERT

The time-lapse ERT measurement yielded a time series of 2-D images of electrical resistivities. For the visualization of changes in the fresh-salt groundwater distribution, and for the comparison with model simulations, these resistivities (inverse is conductivity) were converted to groundwater salinities with the Practical Salinity Scale (PSS) of 1978. The salinity-conductivity relationship in the PSS-1978 is determined by laboratory experiments on (diluted) standard seawater, and is therefore only applicable to water with a similar composition of major ions (viz., Na^+, K^+, Mg^{2+}, Ca^{2+}, Cl^-, HCO_3^-, SO_4^{2-}) as standard seawater. Groundwater salinities at the study site are predominantly a result of the mixing of seawater and rainwater, and will satisfy this requirement to a large extent. However, variations in the chemical composition will probably occur at low salinities (smaller than 2 g TDS L^{-1}), because of the (relatively small) inflow of coastal groundwater and the formation of ions—in particular bicarbonate (HCO_3^-)—by chemical processes. In addition, small errors or variations in the electrical formation factor can result in substantial deviations in the determination of the groundwater conductivities.

This time series of estimated groundwater salinities, and accordingly time-lapse ERT, provided us the instruments to effectively investigate the impact of coastal hydrodynamics and morphodynamics and precipitation on coastal groundwater. The 2-D images contained detailed information on the extent of LSI, and on the change in the fresh-salt groundwater distribution over time. In particular the ability to perform (automated) measurements in multiple dimensions for a period of 2 months was a benefit of the time-lapse ERT. For example, with this method we were able to delineate the extent of multiple inundations with relative accuracy, and coincidentally observe the (2-D) impact on the fresh-salt groundwater distribution. However,

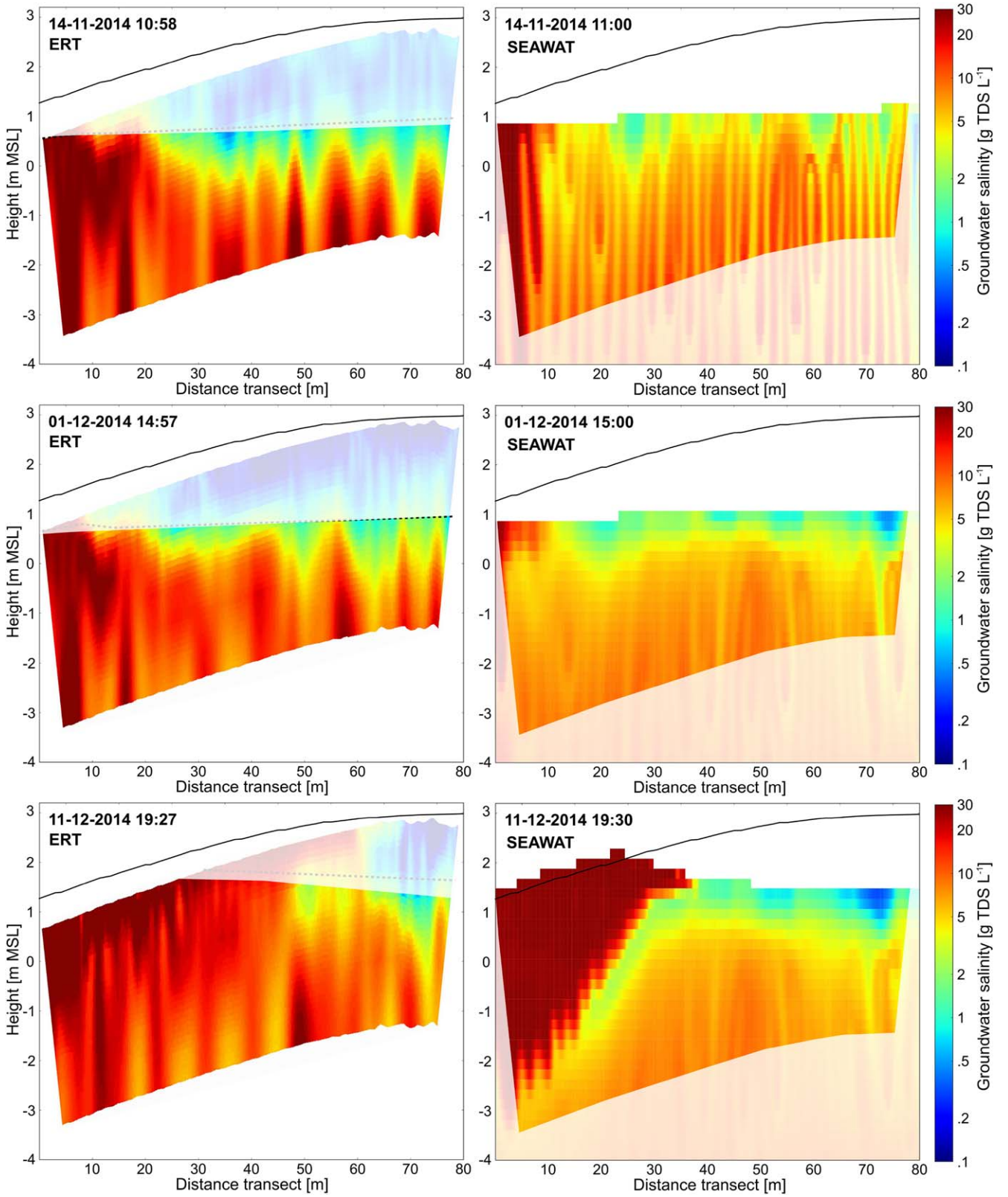

Figure 13. 2-D images of the (left) measured and the (right) simulated groundwater salinity (S3, wave run-up) for three instances: 14 November 11:00 (start of measurements); 1 December 15:00 (after a calm weather period); and 11 December 19:30 (after substantial inundations). These instances are also indicated in Figure 11 and Figure 12 with letters A, B, and C.

an aspect that occasionally led to small anomalies is related to the duration of each individual measurement, which varied between 10 and 30 min. Rapid changes in groundwater salinity and saturation levels during individual measurements caused local anomalies in the electrical resistivity.

It should be noted that inversion of resistivity images often results in nonunique solutions of the electrical resistivity, and that the resolution of inverted images decreases with depth. Generally a decrease in resolution leads to a larger deviation from the actual or earth resistivity and a stronger effect of the starting model and chosen regularization criteria on the acquired data. Inundations of the electrode array can also lead to a reduction in the resolution, because the highly conductive surface-water layer causes a preferential flow of the electrical current [*Henderson et al*., 2010]. This was anticipated in this study and therefore we have focused on data that was acquired close to surface, between the groundwater level and a depth of −1 m MSL as described in section 3.3. Potential poor resolutions in inundated segments of the electrode would only be temporary, and the shallow fresh or brackish groundwater lens in these segments would probably become completely saline. In addition, the reliability of the inversion process was substantiated by low RMS errors (smaller than 1%).

4.2. SWI Processes Due to Tides and Storm Surges

The similarity of the measured and simulated groundwater head, extent of LSI, and change in groundwater salinity proves that reliable simulations of the fluctuation of the groundwater head in complex dynamic coastal environments can be conducted with the adopted simulation methodology. With detailed information on fluctuations in sea-level, topography, and precipitation, it was possible to relatively accurately reproduce short and long-term variations in LSI and groundwater salinity with the calibrated variable-density groundwater model. Here, the incorporation of wave setup and especially wave run-up in the simulations led to a substantial improvement in the estimation of the extent of LSI and SWI. This suggests that in areas with gently sloping beach profiles the extent of inundation could be underestimated when wave run-up is neglected, especially during storm surges.

An important cause of the observed differences between measurement and simulations is probably related to the morphological evolution—between the monthly to bimonthly topographic surveys—that was not incorporated in the simulations. This morphological evolution resulted in a gradual retreat of the shoreline (often exacerbated by storm surges) and the formation of sandbars along the outer perimeter of the Sand Engine, which resulted in shifts of the inundated area. These sandbars could have led to a shift in the location where waves break and reduced wave run-up, and (partially) blocked the flow of seawater, especially when sandbars were connected along the shoreline. Thus, small morphological changes can lead to substantial changes in the area of inundation and wave run-up, and therefore have a strong impact on fresh groundwater in coastal aquifers. For the improvement of simulations of groundwater salinity in such dynamic coastal conditions, it is necessary to incorporate more information on the morphological change during storm surges. Thus, for accurate and detailed delineations of the groundwater head and salinity in local dynamic coastal environments, it is recommended to monitor the local topography frequently or to perform accurate morphological simulations.

In general the simulated fresh-salt groundwater distribution matches the observed patterns in the time-lapse ERT images. These are patterns such as the observed development of a small fresh to brackish groundwater lens after the intensive storm in the night of 21–22 October 2014, and the gradual salinization of the aquifer due to repeated LSI. Deviations in absolute groundwater salinities are probably primarily caused by a combination of errors in the inversion (e.g., over smoothing and inversion artifacts, see Appendix A), errors in the conversion of electrical conductivities to groundwater salinities, errors in the wave setup and wave run-up height and related LSI and SWI during storm surges, and errors in the simulated fresh-salt groundwater distribution in the period previous to the measurements. To differentiate the contribution of each of these factors and to improve simulations in these local dynamic coastal environments, it is recommended to perform more extensive measurements of the groundwater salinity. In addition, wave setup and wave run-up height was estimated with empirical run-up formulas, where the infiltration of seawater by wave run-up was roughly estimated. This approach generally improves the simulation of SWI processes in these environments, but refinements in the prediction of the extent of LSI and the infiltrated volume of seawater can lead to further substantial advances. For example, the incorporation of unsaturated zone processes in the approach could improve the estimation of the volume of

seawater that infiltrates during wave run-up, because the infiltration is probably very sensitive to the saturation level.

5. Conclusions

The measurements show that time-lapse ERT can be a valuable and promising technique for the measurement of temporal and spatial changes in groundwater salinity in dynamic coastal environments. ERT can especially be effective in the measurement of rapid processes such as the effects of saltwater overwash and intrusion during and after storm surges. The observed changes in salinity due to groundwater recharge, tidal dynamics, and storm surges could to a large extent be simulated by a variable-density groundwater model, suggesting that given a thorough understanding of the (local) system, groundwater models can be used to make predictions of the effects of tides and storm surges. However, an accurate numerical simulation of the effect of LSI in (topography-limited) dynamic coastal environments, and especially during storm surges, requires detailed information about morphological changes along the coastline and reliable estimates of the extent of wave run-up.

Appendix A: Synthetic Modeling

The resolution of the inverted resistivity images and potential inversion artifacts was evaluated with a synthetic modeling exercise, consisting of the inversion of simplified hypothetical resistivity images [*Henderson et al*., 2010]. In this study, two hypothetical cases with a shallow fresh groundwater lens—representative of the conditions at the study site—were created with a 2-D groundwater model: case 1 with a sea-level height equal to MHW (1.09 m MSL), and case 2 with an LSI (1.1–2.2 m MSL) of the fresh groundwater lens (Table A1).

This 2-D model contained the same hydrogeological properties and model parameters as the calibrated model, as described in section 2.3.3. The implemented model grid was identical to the tomogram: 159 columns with a constant spacing of 0.5 m, 28 layers with a constant thickness of 0.167 m, and a surface elevation that consists of the 160 measured electrode elevations (incorporated as model nodes). The groundwater salinities in unsaturated model cells were set to 0.1 g TDS L^{-1}. Figure A1 shows the simulated groundwater salinity in case 1 and 2.

The generated salinity distributions were converted to resistivities with equation (1), using the same formation factor as described in section 2.2.3 and the assumption that the groundwater conductivity and groundwater salinity are similar. The resulting resistivities were averaged from 27 to 9 model layers, in accordance with the inverse model used in the time-lapse measurements: 159 columns with a constant spacing of 0.5 m, 9 layers with a variable thickness of 0.167–0.833 m. In addition, we added random electrical noise of 1 mV V^{-1} to the inverse models of case 1 and 2 to simulate the field data.

In order to assess the effect of the chosen minimization norm, both cases were inverted with the full least-squares inversion (minimizing in L2 norm) and the full L1 norm inversion (minimizing L1 in norm). In addition, to assess the effect of Lagrangian multipliers, both cases were also inverted with the constant multiplier of 0.1, and the automatic calculation of the multiplier that is based on the Active Constraint Balancing (ACB) technique [*Yi et al*., 2003].

The inverted distributions of the groundwater salinity (Figures A2 and A3) closely resemble the simulated distributions (Figure A1) for both cases; the overall pattern is captured with all chosen minimization norms and with both the automatic (ACB) and constant Lagrangian multiplier. All inversions also seem to result in

Table A1. Model Parameters in Case 1 "MHW" and Case 2 "LSI"

Model Parameter	Case 1 "MHW"	Case 2 "LSI"
Groundwater recharge	1.4 mm d^{-1} + 0.2 g TDS L^{-1}	0.97 μm min^{-1} + 0.2 g TDS L^{-1}
Initial conditions	1.2 m MSL + 28 g TDS L^{-1}	Output of case 1
Inland boundary	1.1 m MSL + fresh/salt groundwater interface at 0.45 m MSL	1.1 m MSL + fresh/salt groundwater interface at 0.45 m MSL
Model period	180 days	360 min/6 h
Sea-level	1.09 m MSL + 28 g TDS L^{-1}	1.1–2.2 m MSL + 28 g TDS L^{-1}

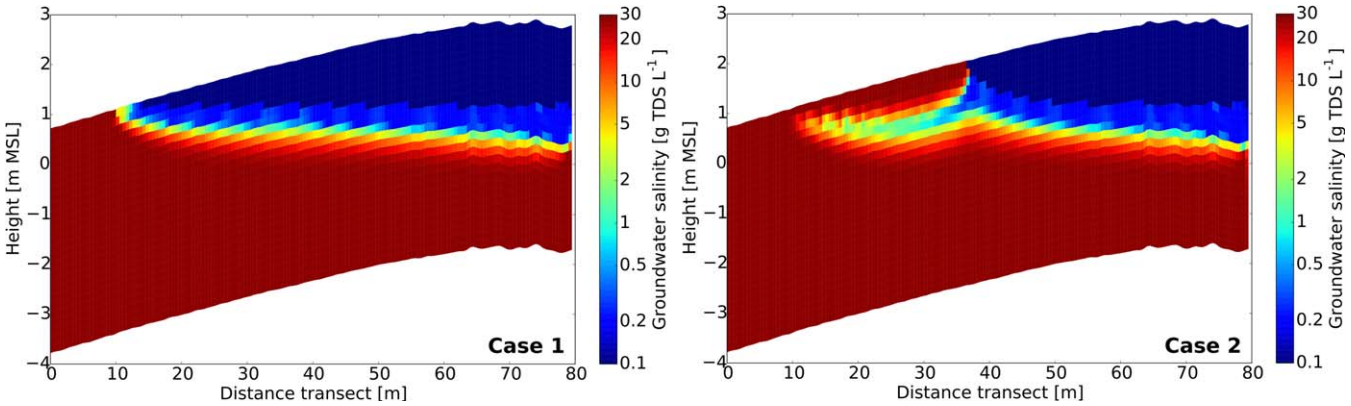

Figure A1. Simulated groundwater salinity of case 1 and 2.

an over smoothing of the simulated fresh-salt groundwater mixing zone, and this effect increases with depth, parallel with the decrease in resolution.

In addition, Figures A2 and A3 show that most vertical features in groundwater salinity near the bottom of images are not present in the simulations, and are probably caused by the decrease in resolution with depth. These inversion artifacts occur with both the L1 and L2 minimization norms, and with the automatic and constant Lagrangian multiplier. However, the images suggest that the automatically calculated Lagrangian multiplier is more vulnerable to these inversion artifacts. For an exact comparison of the inversion methods, we have added the weighted RMS error of the inverse model and the RMS error of the groundwater salinity (inversion compared with simulation) in Table A2. The RMS error is lowest for the L2 norm minimization and the automatic Lagrangian multiplier, but the differences between the inversion methods are small.

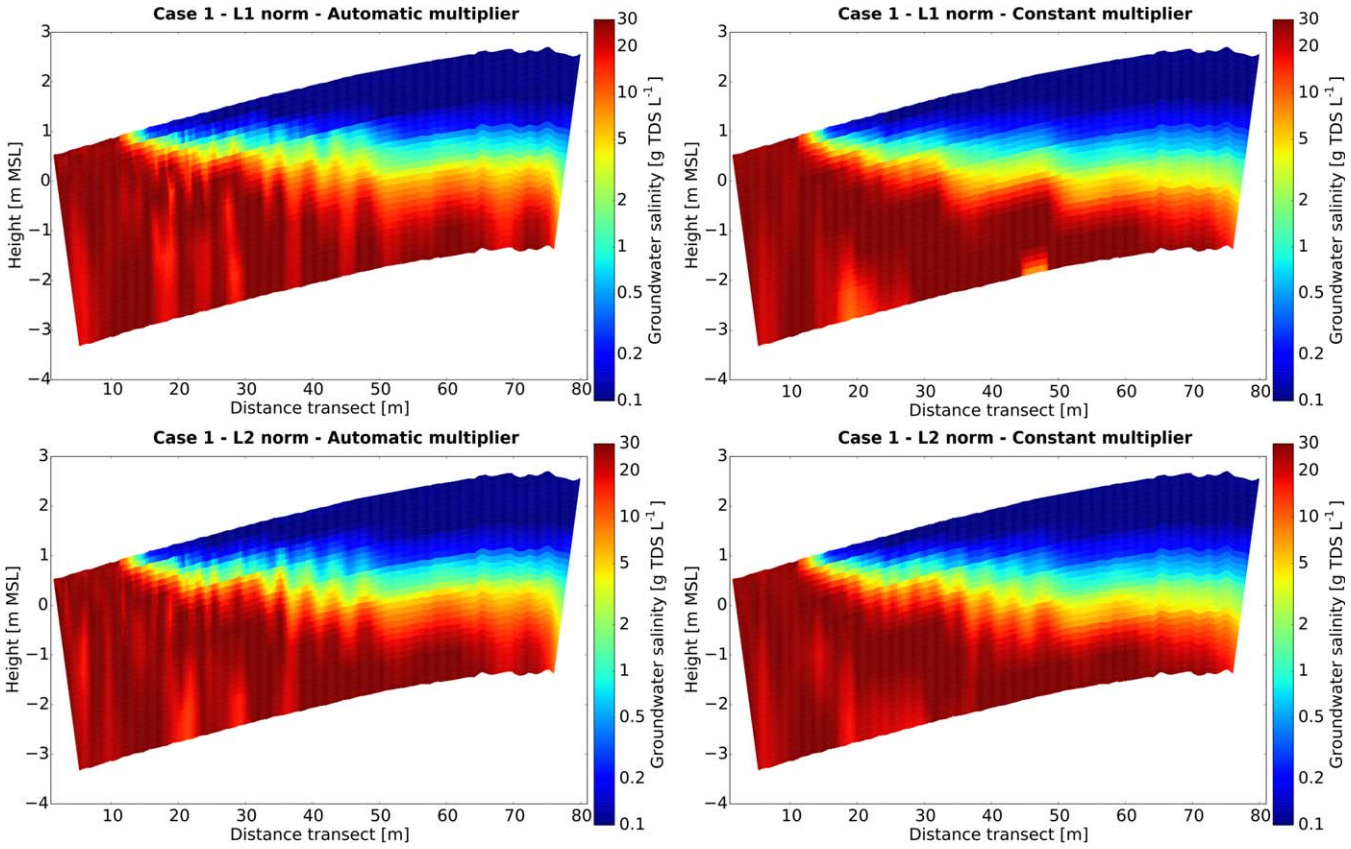

Figure A2. Inverted groundwater salinity of case 1 "MHW," with (top) L1 or (bottom) L2 minimization norms and an (left) automatic or (right) constant Lagrangian multiplier.

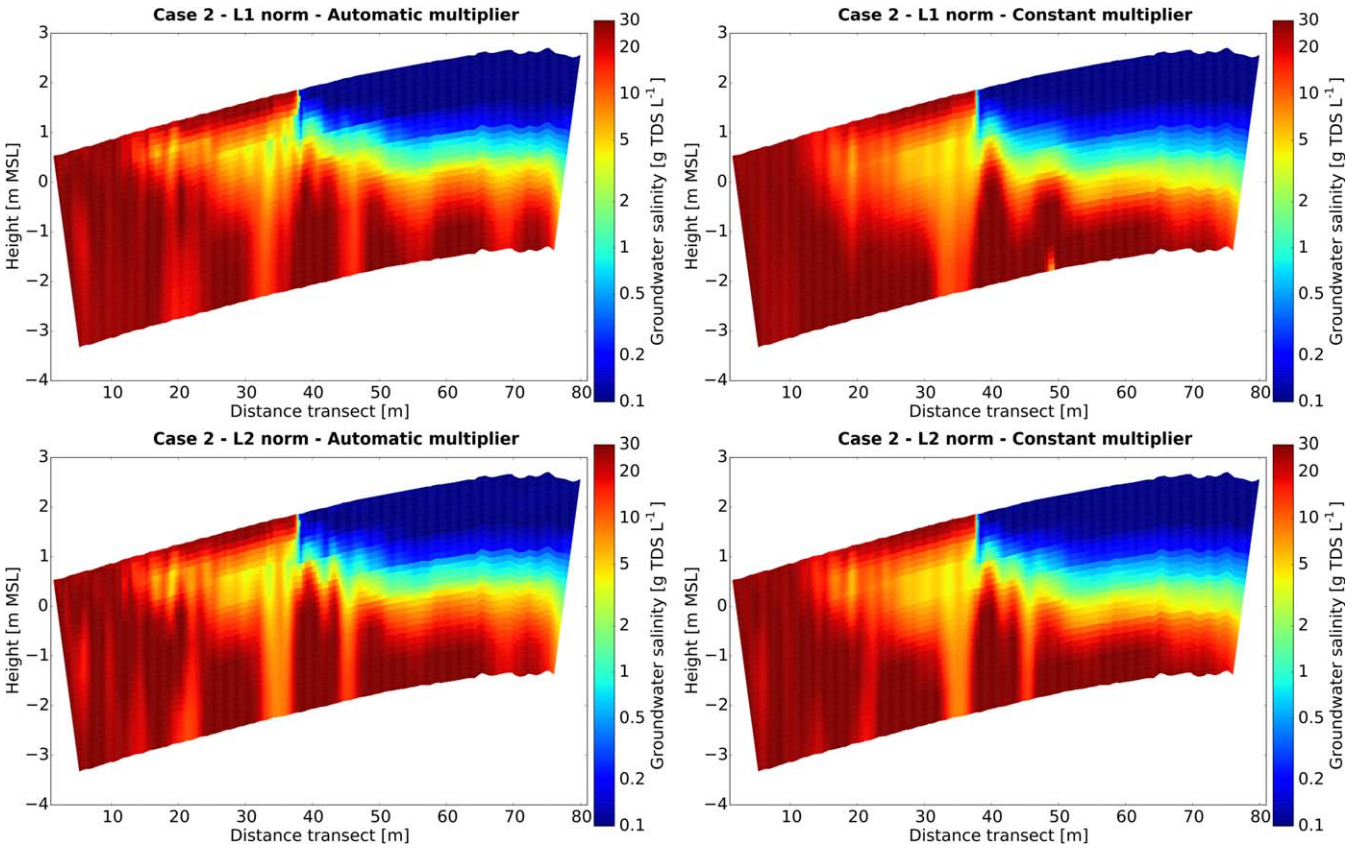

Figure A3. Inverted groundwater salinity of case 2 "LSI," with (top) L1 or (bottom) L2 minimization norms and an (left) automatic or (right) constant Lagrangian multiplier.

Table A2. RMS Error of Inverse Model for Case 1 "MHW" and Case 2 "LSI"

	Case 1 "MHW"		Case 2 "LSI"	
Model RMS Error	Inversion	Salinity	Inversion	Salinity
L1 norm minimization Automatic Lagrangian multiplier	5.8%	5.7 g TDS L^{-1}	5.9%	6.4 g TDS L^{-1}
L1 norm minimization Constant Lagrangian multiplier	7.4%	6.5 g TDS L^{-1}	7.0%	6.4 g TDS L^{-1}
L2 norm minimization Automatic Lagrangian multiplier	5.5%	5.7 g TDS L^{-1}	5.6%	6.4 g TDS L^{-1}
L2 norm minimization Constant Lagrangian multiplier	5.7%	5.7 g TDS L^{-1}	5.9%	7.3 g TDS L^{-1}

Acknowledgments

We thank Mike van der Werf, Marco de Kleine, and André Cinjee for their extensive support in the planning, setup, and upkeep of the ERT measurement. This research is supported by the Dutch Technology Foundation STW, which is part of the Netherlands Organization for Scientific Research (NWO), and which is partly funded by the Ministry of Economic Affairs. This work was carried out within the Nature-driven nourishment of coastal systems (NatureCoast) program. The data used to produce the results of this paper may be obtained by contacting the corresponding author.

References

Abarca, E., H. Karam, H. F. Hemond, and C. F. Harvey (2013), Transient groundwater dynamics in a coastal aquifer: The effects of tides, the lunar cycle, and the beach profile, *Water Resour. Res.*, *49*, 2473–2488, doi:10.1002/wrcr.20075.

Anthony, E. J. (2013), Storms, shoreface morphodynamics, sand supply, and the accretion and erosion of coastal dune barriers in the southern North Sea, *Geomorphology*, *199*, 8–21, doi:10.1016/j.geomorph.2012.06.007.

Ataie-Ashtiani, B., R. E. Volker, and D. A. Lockington (1999), Tidal effects on sea water intrusion in unconfined aquifers, *J. Hydrol.*, *216*(1–2), 17–31, doi:10.1016/S0022-1694(98)00275-3.

Ataie-Ashtiani, B., A. D. Werner, C. T. Simmons, L. K. Morgan, and C. Lu (2013), How important is the impact of land-surface inundation on seawater intrusion caused by sea-level rise?, *Hydrogeol. J.*, *21*(7), 1673–1677, doi:10.1007/s10040-013-1021-0.

Bakhtyar, R., D. A. Barry, L. Li, D. S. Jeng, and A. Yeganeh-Bakhtiary (2009), Modeling sediment transport in the swash zone: A review, *Ocean Eng.*, *36*(9–10), 767–783, doi:10.1016/j.oceaneng.2009.03.003.

Beaujean, J., F. Nguyen, A. Kemna, A. Antonsson, and P. Engesgaard (2014), Calibration of seawater intrusion models: Inverse parameter estimation using surface electrical resistivity tomography and borehole data, *Water Resour. Res.*, *50*, 6828–6849, doi:10.1002/2013WR014020.

Chang, S. W., T. P. Clement, M. J. Simpson, and K. K. Lee (2011), Does sea-level rise have an impact on saltwater intrusion?, *Adv. Water Resour.*, *34*(10), 1283–1291, doi:10.1016/j.advwatres.2011.06.006.

Comte, J. C., and O. Banton (2007), Cross-validation of geo-electrical and hydrogeological models to evaluate seawater intrusion in coastal aquifers, *Geophys. Res. Lett.*, *34*, L10402, doi:10.1029/2007GL029981.
de Bruin, H. A. R. (1987), From Penman to Makkink. Evaporation and weather, in *Volume 39, Proceedings and Information*, *Tech. Meet. 44*, pp. 5–31, TNO Comm. on Hydrol. Res., Ede, The Netherlands.
de Franco, R. et al. (2009), Monitoring the saltwater intrusion by time lapse electrical resistivity tomography: The Chioggia test site (Venice Lagoon, Italy), *J. Appl. Geophys.*, *69*(3–4), 117–130, doi:10.1016/j.jappgeo.2009.08.004.
de Schipper, M. A., S. de Vries, G. Ruessink, R. C. de Zeeuw, J. Rutten, C. van Gelder-Maas, and M. J. F. Stive (2016), Initial spreading of a mega feeder nourishment: Observations of the Sand Engine pilot project, *Coast. Eng.*, *111*, 23–38, doi:10.1016/j.coastaleng.2015.10.011.
Ferguson, G., and T. Gleeson (2012), Vulnerability of coastal aquifers to groundwater use and climate change, *Nat. Clim. Change*, *2*(5), 342–345, doi:10.1038/nclimate1413.
Fofonoff, N. P., and R. C. Millard Jr. (1983), Algorithms for computation of fundamental properties of seawater, *UNESCO Tech. Pap. Mar. Sci.*, *44*, 58 p.
Friedman, S. P. (2005), Soil properties influencing apparent electrical conductivity: A review, *Comput. Electron. Agric.*, *46*(1–3 SPEC. ISS.), 45–70, doi:10.1016/j.compag.2004.11.001.
Goes, B. J. M., G. H. P. Oude Essink, R. W. Vernes, and F. Sergi (2009), Estimating the depth of fresh and brackish groundwater in a predominantly saline region using geophysical and hydrological methods, zeeland, the netherlands, *Near Surf. Geophys.*, *7*(5–6), 401–412, doi:10.3997/1873-0604.2009048.
Heiss, J. W., and H. A. Michael (2014), Saltwater-freshwater mixing dynamics in a sandy beach aquifer over tidal, spring-neap, and seasonal cycles, *Water Resour. Res.*, *50*, 6747–6766, doi:10.1002/2014WR015574.
Henderson, R. D., F. D. Day-Lewis, E. Abarca, C. F. Harvey, H. N. Karam, L. Liu, and J. W. J. Lane (2010), Marine electrical resistivity imaging of submarine groundwater discharge: Sensitivity analysis and application in Waquoit Bay, Massachusetts, USA, *Hydrogeol. J.*, *18*(1), 173–185, doi:10.1007/s10040-009-0498-z.
Hermans, T., A. Vandenbohede, L. Lebbe, R. Martin, A. Kemna, J. Beaujean, and F. Nguyen (2012), Imaging artificial salt water infiltration using electrical resistivity tomography constrained by geostatistical data, *J. Hydrol.*, *438 439–*, 168–180, doi:10.1016/j.jhydrol.2012.03.021.
Hill, K. D., T. M. Dauphinee, and D. J. Woods (1986), The extension of the Practical Salinity Scale 1978 to low salinities, *IEEE J. Ocean. Eng.*, *11*(1), 1–4, doi:10.1109/JOE.1986.1145154.
Holding, S., and D. M. Allen (2015), From days to decades: Numerical modelling of freshwater lens response to climate change stressors on small low-lying islands, *Hydrol. Earth Syst. Sci.*, *19*(2), 933–949, doi:10.5194/hess-19-933-2015.
Huizer, S., G. H. P. Oude Essink, and M. F. P. Bierkens (2016), Fresh groundwater resources in a large sand replenishment, *Hydrol. Earth Syst. Sci.*, *20*, 3149–3166, doi:10.5194/hess-2016-5.
IOC, SCOR, and IAPSO (2010), Appendix E: Algorithm for calculating practical salinity, in *The International Thermodynamic Equation of Seawater–2010: Calculation and Use of Thermodynamic Properties*, pp. 147–151, UNESCO.
Karaoulis, M. C., J.-H. Kim, and P. I. Tsourlos (2011), 4D active time constrained resistivity inversion, *J. Appl. Geophys.*, *73*(1), 25–34, doi:10.1016/j.jappgeo.2010.11.002.
Ketabchi, H., D. Mahmoodzadeh, B. Ataie-Ashtiani, A. D. Werner, and C. T. Simmons (2014), Sea-level rise impact on fresh groundwater lenses in two-layer small islands, *Hydrol. Processes*, *28*(24), 5938–5953, doi:10.1002/hyp.10059.
Ketabchi, H., D. Mahmoodzadeh, B. Ataie-ashtiani, and C. T. Simmons (2016), Sea-level rise impacts on seawater intrusion in coastal aquifers: Review and integration, *J. Hydrol.*, *535*, 235–255, doi:10.1016/j.jhydrol.2016.01.083.
Khan, S. J., D. Deere, F. D. L. Leusch, A. Humpage, M. Jenkins, and D. Cunliffe (2015), Extreme weather events: Should drinking water quality management systems adapt to changing risk profiles?, *Water Res.*, *85*, 124–136, doi:10.1016/j.watres.2015.08.018.
Kim, J. H., M. J. Yi, S. G. Park, and J. G. Kim (2009), 4-D inversion of DC resistivity monitoring data acquired over a dynamically changing earth model, *J. Appl. Geophys.*, *68*(4), 522–532, doi:10.1016/j.jappgeo.2009.03.002.
Kim, J. H., R. Supper, P. Tsourlos, and M. J. Yi (2013), Four-dimensional inversion of resistivity monitoring data through Lp norm minimizations, *Geophys. J. Int.*, *195*(3), 1640–1656, doi:10.1093/gji/ggt324.
Kuan, W. K., G. Jin, P. Xin, C. Robinson, B. Gibbes, and L. Li (2012), Tidal influence on seawater intrusion in unconfined coastal aquifers, *Water Resour. Res.*, *48*, W02502, doi:10.1029/2011WR010678.
Kuras, O., J. D. Pritchard, P. I. Meldrum, J. E. Chambers, P. B. Wilkinson, R. D. Ogilvy, and G. P. Wealthall (2009), Monitoring hydraulic processes with automated time-lapse electrical resistivity tomography (ALERT), *C. R. Geosci.*, *341*(10–11), 868–885, doi:10.1016/j.crte.2009.07.010.
Langevin, C. D., D. T. Thorne Jr., A. Dausman, M. C. Sukop, and W. Guo (2008), SEAWAT version 4: A computer program for simulation of multi-species solute and heat transport, in *U.S. Geological Survey Techniques and Methods Book 6, Chap. A22*, p. 39, U.S. Geol. Surv., Reston, Va.
Levanon, E., E. Shalev, Y. Yechieli, and H. Gvirtzman (2016), Fluctuations of fresh-saline water interface and of water table induced by sea tides in unconfined aquifers, *Adv. Water Resour.*, *96*, 34–42, doi:10.1016/j.advwatres.2016.06.013.
Liu, Y., S. Shang, and X. Mao (2012), Tidal effects on groundwater dynamics in coastal aquifer under different beach slopes, *J. Hydrodyn. Ser. B*, *24*(1), 97–106, doi:10.1016/S1001-6058(11)60223-0.
Mao, X., P. Enot, D. A. Barry, L. Li, A. Binley, and D. S. Jeng (2006), Tidal influence on behaviour of a coastal aquifer adjacent to a low-relief estuary, *J. Hydrol.*, *327*(1–2), 110–127, doi:10.1016/j.jhydrol.2005.11.030.
McDonald, M. G., A. W. Harbaugh, B. R. Orr, and D. J. Ackerman (1992), A method of converting no-flow cells to variable- head cells for the U.S. Geological Survey modular finite-difference ground-water flow model, *U.S. Geol. Surv. Open File Rep.*, *91–536*, 99 p.
McGranahan, G., D. Balk, and B. Anderson (2007), The rising tide: Assessing the risks of climate change and human settlements in low elevation coastal zones, *Environ. Urban.*, *19*(1), 17–37, doi:10.1177/0956247807076960.
Meinardi, C. R. (1994), Groundwater recharge and travel times in the sandy regions of the Netherlands, PhD thesis, VU Univ. Amsterdam, Amsterdam, Netherlands.
Michael, H. A., C. J. Russoniello, and L. A. Byron (2013), Global assessment of vulnerability to sea-level rise in topography-limited and recharge-limited coastal groundwater systems, *Water Resour. Res.*, *49*, 2228–2240, doi:10.1002/wrcr.20213.
Millero, F. J., R. Feistel, D. G. Wright, and T. J. McDougall (2008), The composition of Standard seawater and the definition of the reference-composition salinity scale, *Deep Sea Res. Part I*, *55*(1), 50–72, doi:10.1016/j.dsr.2007.10.001.
Morgan, L. K., and A. D. Werner (2014), Seawater intrusion vulnerability indicators for freshwater lenses in strip islands, *J. Hydrol.*, *508*, 322–327, doi:10.1016/j.jhydrol.2013.11.002.
Morrow, F. J., M. R. Ingham, and J. A. McConchie (2010), Monitoring of tidal influences on the saline interface using resistivity traversing and cross-borehole resistivity tomography, *J. Hydrol.*, *389*(1–2), 69–77, doi:10.1016/j.jhydrol.2010.05.022.

Mulder, J. P. M., and P. K. Tonnon (2011), "Sand Engine": Background and Design of a Mega-Nourishment Pilot in The Netherlands, *Coast. Eng. Proc.*, *1*(32), 1–10, doi:10.9753/icce.v32.management.35.
Mulligan, A. E., C. D. Langevin, and V. E. A. Post (2011), Tidal boundary conditions in SEAWAT., *Ground Water*, *49*(6), 866–79, doi:10.1111/j.1745-6584.2010.00788.x.
Nguyen, F., a. Kemna, a. Antonsson, P. Engesgaard, O. Kuras, R. Ogilvy, J. Gisbert, S. Jorreto, and A. Pulido-Bosch (2009), Characterization of seawater intrusion using 2D electrical imaging, *Near Surf. Geophys.*, *7*(5–6), 377–390, doi:10.3997/1873-0604.2009025.
Nicholls, R. J. (2010), Impacts of and responses to Sea-Level Rise, in *Understanding Sea-Level Rise and Variability*, edited by J. A. Church et al., pp. 17–51, Wiley-Blackwell, Oxford, U. K.
Ogilvy, R. D. et al. (2009), Automated monitoring of coastal aquifers with electrical resistivity tomography, *Near Surf. Geophys.*, *7*(5–6), 367–375, doi:10.1007/s13398-014-0173-7.2.
Oude Essink, G. H. P., E. S. van Baaren, and P. G. B. de Louw (2010), Effects of climate change on coastal groundwater systems: A modeling study in the Netherlands, *Water Resour. Res.*, *46*, W00F04, doi:10.1029/2009WR008719.
Pauw, P. S., G. H. P. Oude Essink, A. Leijnse, A. Vandenbohede, J. Groen, and S. E. A. T. M. van der Zee (2014), Regional scale impact of tidal forcing on groundwater flow in unconfined coastal aquifers, *J. Hydrol.*, *517*, 269–283, doi:10.1016/j.jhydrol.2014.05.042.
Post, V. E. A. (2012), Electrical conductivity as a proxy for groundwater density in coastal aquifers, *Ground Water*, *50*(5), 785–92, doi:10.1111/j.1745-6584.2011.00903.x.
Revil, A., M. Karaoulis, T. Johnson, and A. Kemna (2012), Review: Some low-frequency electrical methods for subsurface characterization and monitoring in hydrogeology, *Hydrogeol. J.*, *20*(4), 617–658, doi:10.1007/s10040-011-0819-x.
Rijkswaterstaat (2012), Salinity in the North Sea along the coast [in Dutch], in North Sea Atlas, Part I: Water Syst., IDON. [Available at http://www.noordzeeloket.nl/en/spatial-management/north-sea-atlas/watersysteem/zoutgehalte.aspx.]
Robinson, C., L. Li, and D. A. Barry (2007a), Effect of tidal forcing on a subterranean estuary, *Adv. Water Resour.*, *30*(4), 851–865, doi:10.1016/j.advwatres.2006.07.006.
Robinson, C., L. Li, and H. Prommer (2007b), Tide-induced recirculation across the aquifer-ocean interface, *Water Resour. Res.*, *43*, W07428, doi:10.1029/2006WR005679.
Rutten, J., S. M. de Jong, and G. Ruessink (2017), Accuracy of nearshore bathymetry inverted from X-band radar and optical video data, *IEEE Trans. Geosci. Remote Sens.*, *55*(2), 1106–1116, doi:10.1109/TGRS.2016.2619481.
Spieksma, J. F. M., A. J. Dolman, and J. M. Schouwenaars (1996), National Research program Dehydration: The parameterisation of the evapotranspiration of natural areas in hydrological models [in Dutch], pp. 99, Nationaal Onderzoeksprogramma Verdroging (NOV), Zoetermeer, Netherlands.
Stockdon, H. F., R. A. Holman, P. A. Howd, and A. H. Sallenger (2006), Empirical parameterization of setup, swash, and runup, *Coast. Eng.*, *53*(7), 573–588, doi:10.1016/j.coastaleng.2005.12.005.
Vallejos, A., F. Sola, and A. Pulido-Bosch (2014), Processes influencing groundwater level and the freshwater-saltwater interface in a coastal aquifer, *Water Resour. Manage.*, *29*(3), 679–697, doi:10.1007/s11269-014-0621-3.
Watson, T. A., A. D. Werner, and C. T. Simmons (2010), Transience of seawater intrusion in response to sea level rise, *Water Resour. Res.*, *46* W12533, doi:10.1029/2010WR009564.
Waxman, M. H., and L. J. M. Smits (1968), Electrical conductivities in oil-bearing shaly sands, *Soc. Pet. Eng. J.*, *8*(2), 107–122.
Webb, M. D., and K. W. F. Howard (2011), Modeling the transient response of saline intrusion to rising sea-levels, *Ground Water*, *49*(4), 560–569, doi:10.1111/j.1745-6584.2010.00758.x.
Werner, A. D., M. Bakker, V. E. A. Post, A. Vandenbohede, C. Lu, B. Ataie-Ashtiani, C. T. Simmons, and D. A. Barry (2013), Seawater intrusion processes, investigation and management: Recent advances and future challenges, *Adv. Water Resour.*, *51*, 3–26, doi:10.1016/j.advwatres.2012.03.004.
Wilson, A. M., W. S. Moore, S. B. Joye, J. L. Anderson, and C. A. Schutte (2011), Storm-driven groundwater flow in a salt marsh, *Water Resour. Res.*, *47*, W02535, doi:10.1029/2010WR009496.
Wong, P. P., I. J. Losada, J.-P. Gattuso, J. Hinkel, A. Khattabi, K. L. McInnes, Y. Saito, and A. Sallenger (2014), Coastal systems and low-lying areas, in *Climate Change 2014: Impacts, Adaptation, and Vulnerability. Part A: Global and Sectoral Aspects. Contribution of Working Group II to the Fifth Assessment Report of the Intergovernmental Panel on Climate Change*, pp. 361–409, Cambridge Univ. Press, Cambridge, U. K.
Yang, J., T. Graf, M. Herold, and T. Ptak (2013), Modelling the effects of tides and storm surges on coastal aquifers using a coupled surface–subsurface approach, *J. Contam. Hydrol.*, *149*, 61–75, doi:10.1016/j.jconhyd.2013.03.002.
Yi, M.-J., J.-H. Kim, and S.-H. Chung (2003), Enhancing the resolving power of least squares inversion with active constraint balancing, *Geophysics*, *68*(3), 931–941, doi:10.1190/1.1581045.
Zhang, Y., L. Li, D. V. Erler, I. R. Santos, and D. A. Lockington (2016), Effect of alongshore morphology on groundwater flow and solute transport in a nearshore aquifer, *Water Resour. Res.*, *52*, 990–1008, doi:10.1002/2014WR015716.